



Barbara Glanzer, BSc

**Development and characterization  
of mechanically deposited graphene  
functionalized porous copper layers**

**MASTER'S THESIS**

to achieve the university degree of

Diplom-Ingenieurin

Master's degree programme: Advanced Materials Science

submitted to

**Graz University of Technology**

Supervisor

Ao.Univ.-Prof. Mag. Dr.rer.nat. Robert Schennach

Institute of Solid State Physics

## **AFFIDAVIT**

I declare that I have authored this thesis independently, that I have not used other than the declared sources/resources, and that I have explicitly indicated all material which has been quoted either literally or by content from the sources used. The text document uploaded to TUGRAZonline is identical to the present master's thesis.

---

Date

---

Signature

## Abstract

The aim of this project was to investigate the influence of graphene used as compound material in porous copper systems applied in semiconductor industry. Thus different combinations of copper pastes consisting of micro-nano or nano copper particles, organic particle coatings, solvents and varying graphene content and graphene qualities were applied on silicon wafers using stencil printing technique to deposit a metal layer in the size range of a few to a few hundred micrometers.

Subsequently the fluid copper-graphene pastes were solidified in a furnace at 400 °C and in reducing atmosphere, resulting in an interconnected porous copper network with graphene agglomerations located in the pores.

Two different approaches were focused regarding the development of pasty copper-graphene materials: stirring of dissolved graphene powder into a well-characterized copper paste and characterization or rather optimization of noble copper pastes to select an adequate basic copper system for consequently manufactured copper-graphene pastes of an external provider. Compared to the material properties of the reference (micro-)nano pastes consisting of the same basic copper paste system, but without graphene content, the copper-graphene compounds show similar results concerning specific resistivity (range from 3-4  $\mu\Omega cm$ ), CTE and stress behavior.

All investigated compound systems were processed and characterized equally, including analysis methods such as profilometry, four-point probing, scanning electron microscopy, energy-dispersive X-ray, thermomechanical analysis, dynamic mechanical analysis, wafer bow measurements and Raman spectroscopy.

## Acknowledgements

I want to thank

- Robert Schennach, my supervisor at TU Graz.
- Martin Mischitz, my supervisor at Infineon Austria.
- Barbara Eichinger, my supervising PhD-student.
- all my friends who helped me overcome every obstacle and with whom I enjoy life together.
- my best friend to whom I am infinitely thankful for our time spent together. You will stay unforgotten.
- my partner for his love and affection, which strengthen me on a personal level and for his support and encouraging nature.
- my family, especially my parents who not only enabled me a light-hearted and merry student's life with their financial support, but also for smoothing me a way with their affectionate and kind education that facilitates development on a professional and personal level. Additionally, I want to thank them for the love they display daily and for being always able to rely on them.

# Contents

<b>1</b>	<b>Introduction</b>	<b>1</b>
<b>2</b>	<b>Theoretical Background</b>	<b>3</b>
2.1	Porous copper systems . . . . .	3
2.2	Graphene . . . . .	6
2.2.0.1	Synthesis of graphene [8] . . . . .	7
2.2.0.1.1	Mechanical exfoliation [8] . . . . .	7
2.2.0.1.2	Chemical exfoliation [8] . . . . .	7
2.2.0.1.3	Chemical vapour deposition [8] . . . . .	7
2.2.0.2	Properties of graphene . . . . .	8
2.3	Processing . . . . .	8
2.3.1	Paste material and wafer stack . . . . .	8
2.3.2	Printing . . . . .	9
2.3.3	Drying . . . . .	11
2.3.4	Curing . . . . .	12
2.4	Characterization Methods . . . . .	17
2.4.1	Standardized characterization . . . . .	17
2.4.1.1	Solids content . . . . .	17
2.4.1.2	Specific Resistivity . . . . .	18
2.4.1.2.1	Electrical and thermal conductivity in metals . . . . .	18
2.4.1.2.2	Four-point probe method . . . . .	19
2.4.1.3	Layer Thickness . . . . .	20
2.4.1.3.1	Scanning probe microscopy - Profilometer . . . . .	20
2.4.1.3.2	Sample preparation for layer thickness measurements	20
2.4.1.4	Porosity . . . . .	21
2.4.2	Scanning Electron Microscopy . . . . .	22
2.4.2.1	Energy dispersive x-ray spectroscopy . . . . .	24
2.4.3	Focused Ion Beam . . . . .	24
2.4.4	Thermomechanical Analysis . . . . .	25
2.4.5	Dynamic Mechanical Analysis . . . . .	26

---

2.4.6	Wafer bow measurements . . . . .	27
2.4.7	Raman spectroscopy . . . . .	28
2.4.7.1	Determination of stress states in the silicon substrate . . . . .	28
2.4.7.2	Classification of graphene . . . . .	29
<b>3</b>	<b>Experiments and Evaluation</b>	<b>30</b>
3.1	Characterization of pure copper particle pastes . . . . .	30
3.2	Development and characterization of copper-graphene pastes . . . . .	32
3.2.1	Mixing of copper paste and powdery graphene . . . . .	32
3.2.2	Evaluation of provided copper-graphene pastes . . . . .	36
3.2.2.1	Nano copper particle pastes with graphene content . . . . .	37
3.2.2.2	Micro-nano copper particle pastes with graphene content . . . . .	45
3.2.2.3	Characterization of remaining copper-graphene pastes . . . . .	52
3.3	Raman spectroscopy of the silicon substrate . . . . .	57
<b>4</b>	<b>Summary and Conclusion</b>	<b>60</b>

# List of Figures

2.1	Relation between porosity and conductivity performance. Source:[4]	5
2.2	Relation between porosity and conductivity performance. Source:[5]	6
2.3	TEM image of a graphene sheet illustrating the crystalline lattice . Source: [7]	7
2.4	Outline of paste movement during printing process. Source: [11]	9
2.5	Schematic overview of the stencil printing technique. [11]	10
2.6	DEK printer assembly. Source: [12]	11
2.7	View on the insight of the <i>YES</i> furnace	12
2.8	(a) ATV furnace with vacuum pump and cooling system. (b) Furnace chamber. Source: [13]	13
2.9	Main steps of a process using 400 °C as maximum temperature.	14
2.10	Process flow of the recipe: 400-000	15
2.11	Process flow of the recipe: 400-060	15
2.12	Process flow of the recipe: 400-180	16
2.13	Positions of samples used for standardized characterization.	17
2.14	Four-point probe measurement. Source: [19]	19
2.15	Mechanical profilometer. Source: [21]	20
2.16	Etching pattern and scheme of expected corresponding height profile.	21
2.17	Principle of a scanning electron microscope. Source: [23]	23
2.18	Scanning electron microscope - interaction volume. Source: [24]	24
2.19	Principle of a dual-beam FIB-SEM instrument. Source: [26]	25
2.20	Principle of a thermomechanical analysis. Source: [29]	26
2.21	Principle of a dynamic mechanical analysis. Source: [30]	27
2.22	Comparison of the Raman spectra of graphene and graphite measured at 514.5 nm. Source: [36]	29
3.1	Results of copper particle pastes regarding the relation of porosity and resistivity.	31
3.2	Comparison of wafer color after drying (left) and after curing (right). Source: [13]	31
3.3	Surface discoloration effect on samples of paste 2B3 and 5B2 (wafer piece).	32

3.4	(a) Cross-section of materials grade graphene, 1 wt.-% sample. (b) Top-view of materials grade, 1 wt.-% sample . . . . .	34
3.5	Stress behavior of self-mixed paste. . . . .	35
3.6	Raman spectrum of self-mixed paste. . . . .	36
3.7	Measured specific resistivity data. . . . .	38
3.8	(a) Top view of pure copper reference paste. (b) Top view of paste D. . . . .	39
3.9	(a) Cross section of pure copper reference paste. (b) Cross section of paste D. . . . .	40
3.10	(a) SEM of FIB cut of paste D. (b) Magnified graphene agglomeration. . . . .	41
3.11	Raman spectrum of paste D. . . . .	42
3.12	CTE measurements of paste D. . . . .	43
3.13	Stress measurements of paste D. . . . .	44
3.14	Dynamic mechanical analysis of paste D. . . . .	45
3.15	Specific resistivity values of micro-nano copper particle pastes with different graphene content and quality. . . . .	45
3.16	(a) Top view of pure copper reference paste. (b) Top view of paste H. . . . .	47
3.17	(a) Cross section of pure copper reference paste. (b) Cross section of paste H. . . . .	48
3.18	(a) SEM of FIB cut of paste H. (b) Magnified graphene agglomeration. . . . .	49
3.19	EDX-Analysis of paste H. Orange colored copper and green colored graphene/carbon located predominately in pores. . . . .	50
3.20	Raman spectrum of paste H. . . . .	50
3.21	CTE measurements of paste H. . . . .	51
3.22	DMA results of paste H. . . . .	52
3.23	(a) Top view of paste A. (b) Cross section of paste A. . . . .	53
3.24	(a) Top view of paste B. (b) Cross section of paste B. . . . .	54
3.25	Top view SEM image of paste E. . . . .	55
3.26	Top view SEM image of paste G. . . . .	56
3.27	Stress states of silicon substrate after different methods of metallization deposition. . . . .	58
3.28	Stress states of silicon substrate after processing of paste H. . . . .	59
4.1	Stress measurements of paste <i>A</i> (a), paste <i>B</i> (b) and paste <i>C</i> (c). . . . .	62
4.2	Stress measurements of CP with 1 wt.% materials grade graphene (a) and CP with 5 wt.% materials grade graphene (b). . . . .	63
4.3	CTE measurements of paste <i>A</i> (a) and paste <i>B</i> (b). . . . .	63
4.4	CTE measurements of paste <i>D</i> (a) and paste <i>H</i> (b). . . . .	64
4.5	Young's modulus measurements of paste <i>D</i> (a) and paste <i>H</i> (b). . . . .	64

# List of Tables

2.1	Generally used printing parameters . . . . .	11
2.2	Description of the main steps during a curing process. . . . .	14
2.3	Description of curing process: 400-000 . . . . .	16
2.4	Description of curing process: 400-060 . . . . .	16
2.5	Description of curing process: 400-180 . . . . .	17
3.1	Results of copper particle pastes . . . . .	30
3.2	Results of optimized copper particle pastes . . . . .	32
3.3	Results concerning specific resistivity performance of self-mixed copper-graphene pastes . . . . .	33
3.4	Combinations of self-mixed copper-graphene pastes . . . . .	33
3.5	Combinations of self-mixed copper-graphene pastes . . . . .	35
3.6	Overview of readily provided pastes . . . . .	37
3.7	Average specific resistivity values of pastes <i>A-D</i> compared to the reference . . . . .	38
3.8	Results of stress measurements of paste D. . . . .	44
3.9	Average specific resistivity values of pastes <i>E-H</i> compared to the reference paste . . . . .	46
3.10	Results of stress measurements of paste A. . . . .	53
3.11	Overview of wafers characterized by Raman spectroscopy. . . . .	58
4.1	Overview of measured results. . . . .	65

# Abbreviations

BSE	Back Scattered Electrons
CTE	Coefficient of Thermal Expansion
CVD	Chemical Vapor Deposition
DMA	Dynamic Mechanical Analysis
ECD	Electro Chemical Deposition
EDX	Energy Dispersive X-ray Spectroscopy
FAV	Formic Acid Vapor
FIB	Focused Ion Beam
HMDS	HexaMethylDiSilazane
LPNC	Low Porosity Nano Crystalline
LVDT	Linear Variable Differential Transformer
PVD	Physical Vapor Deposition
RT	Room Temperature
SE	Secondary Electrons
SEM	Scanning Electron Microscopy
TMA	Thermo Mechanical Analysis

# Chapter 1

## Introduction

During the last few years graphene was established as one of the most popular materials used as a composite. Depending on the field of application graphene is attractive due to a wide array of different basic properties. Since research about graphene has advanced considerably, the question arises whether graphene could be beneficial for semiconductor devices.

Considering, for example, the assembly of a chip integrated in circuits used in daily inevitable commodities like vehicles, chip-cards or phones, there are many layers of varying functional materials. Besides diffusion or barrier layers, also thermal conductive layers represent an important part of the entire stack.

In semiconductor industry, there are many different methods to deposit conducting metal layers on the front- or backside of a device. These layers serve as heat dissipators that transfer device determined heat to reduce relating resistivity. Other than the most commonly used methods like electro-chemical deposition or physical vapour deposition, there are less developed, but highly innovative techniques like metal deposition by stencil printing using high viscous materials, such as metal pastes. The composition of the pastes ensures that after a heat treatment step up to 400°C all chemical additives evaporate and only a structure of sintered metal particles remains. The main motivations for further investigations and development of this procedure are advantages over ECD or PVD such as cost reduction, fast deposition of thick layers in a range of a few to a few hundred micrometers, as well as stress reduction between the layer interfaces due to a porous system for similar thermal and electrical conductivity values and so on. In addition, porous copper systems are also related to some negative aspects, such as reduced conductivity and a higher surface roughness compared to non-porous bulk copper, leading to complications with subsequent production steps such as wire bonding. The procedure itself at its current state further entails some challenging factors, such as choosing the proper printing setup and optimizing conditions for subsequent heat treatments.

Combining graphene in terms of a single or few layer material with copper pastes is based on the consideration to enhance the properties of the printed porous copper layers with some of the typical characteristics of graphene, such as an excellent thermal/electrical conductivity, a low coefficient of thermal expansion and high intrinsic strength. Consequently, these advantages could lead to a better heat dissipation, less defects like cracks, voids or delamination on the interface between the functionalized silicon wafer and the metallization layer due to a CTE mismatch reduction between the metallization layer and the silicon. Further improvements are expected regarding the stability of the metallization layer itself - the high intrinsic strength of graphene could enhance the hardness of the layer and could improve its durability under external influences.

Concluding, the aim of this project is to quantify and qualify the effect of graphene used as a composite material in porous copper systems. The main focus is to consider relevant properties and to gain a deeper knowledge about the system's electric/thermal performance, as well as microstructural changes due to the stress behaviour between the interface of the silicon and the copper-graphene layer itself. Additionally, the impact of the graphene content as well as the number of layers on porous copper-graphene composites is investigated.

## Chapter 2

# Theoretical Background

### 2.1 Porous copper systems

Generally, a porous material consists of a continuous solid phase and gaseous pores. Pores have advantageous effects on the material's properties in contrast to vacancies or voids which are classified as defects since the material's performance is lowered. Porous materials can be divided into open- and closed porous systems, depending on how the pores are enclosed with respect to the solid frame. Further kinds of classifications concern the pore size and porosity, i.e. the fraction of pore volume to the total volume.

The properties of the porous material compared to its dense counterpart mainly depend on the pore morphology [1, 2]:

- pore size (i.e., the average diameter of the pores and the distribution of pore sizes)
- pore shape
- open- or closed porous system

Basically, there are four types of porous materials including porous ceramics, porous polymers, porous metals and porous composites. Further on, only porous metals (copper) and porous composites (copper-graphene) will be discussed. Research on the low- to mid-level porosity range is often performed with copper, since it is comparably easy to process due to its low melting point, displays highly ductile stress-strain behaviour as well as high electrical and thermal conductivity and is relatively cheap.

To use the benefits mentioned before it has to be ensured that the green body material shows high purity and is totally sintered. The driving force of the sintering process is defined as the reduction of the total free energy of the porous system. The activation energy of the sintering process decreases with the size of the basic particles that has to be sintered due to the increasing surface-to-volume ratio. In a first step two particles agglomerate and combine

by forming sintering necks to decrease the specific surface area. Pores which are included inside the metal network can be considered as defects which hinder the formation of a regular crystal lattice and increase the total free energy of the porous body. As a direct effect of the material heating during sintering, grains grow and the shape of the particles changes, reducing the pore volume and surface. Grain growth, reduction of pores and the resulting densification occur by different transport mechanisms: diffusion in the grain boundaries, volume diffusion, surface diffusion and evaporation/recondensation. Due to vacancies and other microstructural defects, grain boundary diffusion already occurs at low temperatures, since small particle sizes promote the diffusion while little activation energy is required. At higher temperatures the porous body shrinks due to volume diffusion of atoms from inside the particles which fill up interstices at the contact surface. So the growth of sintering necks is promoted. Finally, surface diffusion is linked to atoms on the particle surface and subsequently leads to an expansion of the contact area between the particles. The mass transport contributes to the neck growth. Only the grain boundary and volume diffusion contribute to the densification of the porous body. Hence recrystallization and grain growth start which lead to an elimination of crystal lattice distortions and a reduction of the amount of pores and grain boundaries. Generally the sintering process can be divided into the following stages: growing and formation of sintering necks, densification and particulate grain growth [1, 3].

Concerning the previously mentioned high electrical and thermal conductivity values of bulk copper it has to be considered that porous metals show lower electrical/thermal conductivity performances due to the gas-filled pores which have insulating characteristics. A theoretically defined relation between porosity and conductivity of metals can be seen in fig. 2.1 [4].

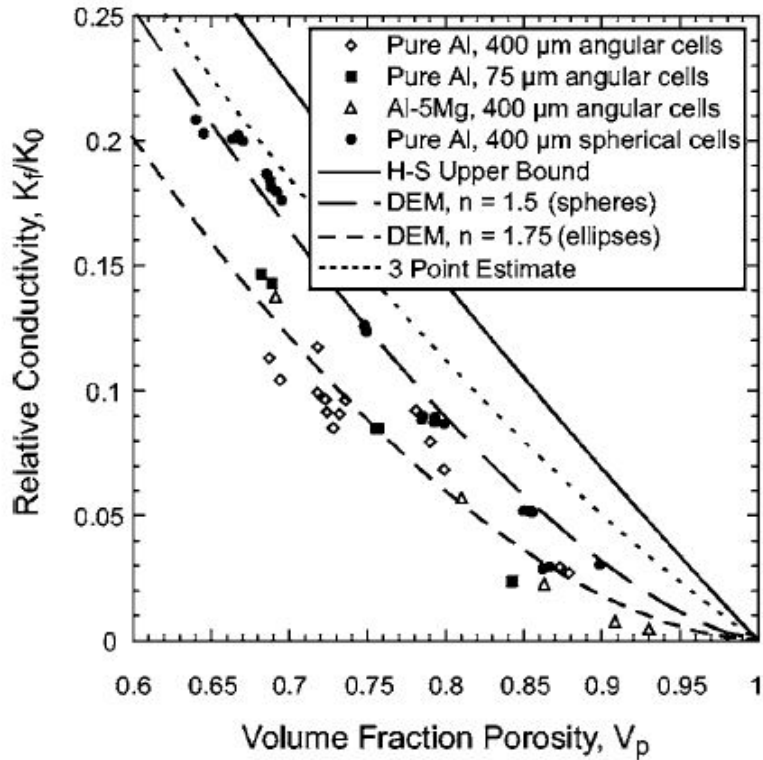


Figure 2.1: Relation between porosity and conductivity performance. Source:[4]

However, porosity has an advantageous influence on the Young's modulus of the material. The Young's modulus ( $E$ ) is defined as the ratio between stress ( $\sigma$ ) and strain ( $\epsilon$ ) up to the Yield point, see eq. (2.1).

$$E = \frac{\sigma}{\epsilon} \quad (2.1)$$

Fig. 2.2 shows the Young's modulus, especially, for porous copper against porosity. The modulus decreases drastically for porosities larger than 10% and thus has special significance for subsequently investigated porous copper systems.

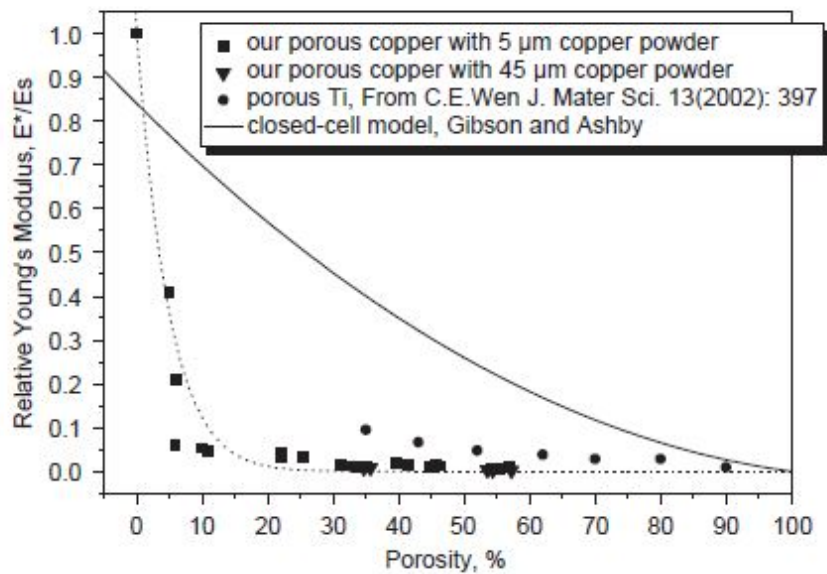


Figure 2.2: Relation between porosity and conductivity performance. Source:[5]

## 2.2 Graphene

Graphene is one of the carbon allotropes currently being intensively researched for different fields of applications. Graphene is a two-dimensional material consisting of hexagonally arranged,  $sp^2$  hybridized, carbon atoms (honeycomb-like structure) which are covalently bonded having a bond length of around 0.142 nm. The layer height of graphene is around 0.3 nm. Additionally, graphene is characterized by a very dense structure so that even very small atoms like helium cannot pass through. One of the most popular properties of graphene used in semiconductor industry is the conduction of electricity which is in the same range as for copper (graphene:  $96 \cdot 10^6 \Omega^{-1}m^{-1}$ , copper:  $58 \cdot 10^6 \Omega^{-1}m^{-1}$ ) [6]. The high electrical conductivity results from delocated electrons in the 2D-plane, due to the  $sp^2$  hybridized carbon atoms. The crystal structure of graphene is shown in fig. 2.3.

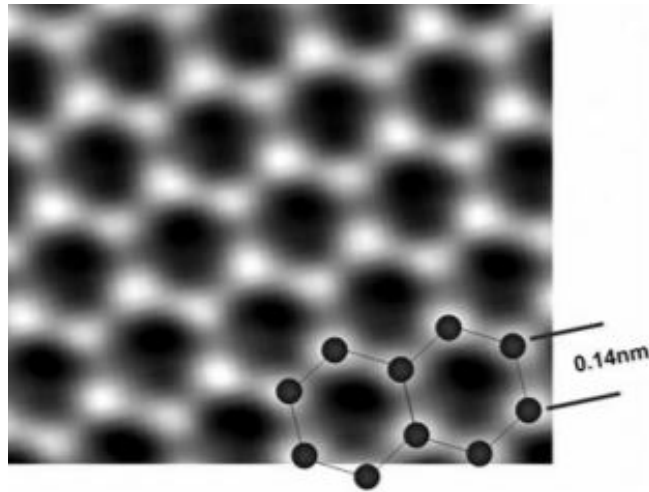


Figure 2.3: TEM image of a graphene sheet illustrating the crystalline lattice . Source: [7]

### 2.2.0.1 Synthesis of graphene [8]

To draw on the special properties of graphene, amongst other things, it must have a small defect density. Researchers seek for methods to produce and provide high quality graphene in high quantities. The subsequent sections give an overview about the basic concepts of how to synthesize graphene.

**2.2.0.1.1 Mechanical exfoliation [8]** Due to extremely high bonding forces between the hexagonal arranged carbon atoms in contrast to weaker bonding forces and large lattice spacing of the carbon in perpendicular direction of graphite it is possible to generate graphene sheets through exfoliation of graphite. This has already been done using, for example, AFM tips.

Mechanical exfoliation produces highest quality graphene (smallest defect density).

**2.2.0.1.2 Chemical exfoliation [8]** Chemical exfoliation is a two-step process and another example for so-called top-down methods which generate graphene out of graphite. First the interlayer van der Waals bonding forces have to be reduced by increasing the interlayer spacing of graphite, e.g. oxidized graphite (increase of the interlayer spacing from 3.7 to 9.5 Å). In a second step, single- or few-layer graphene is exfoliated by rapid heating, sonication or strong shear forces.

Chemical reduction of graphite oxide is generally the most established method to produce graphene in large quantities.

**2.2.0.1.3 Chemical vapour deposition [8]** This procedure is the most promising one to generate high quality graphene in an inexpensive and readily accessible way. Therefore, CVD onto transition metal substrates such as Ni, Pd, Au, Co or Cu is used. The graphene

generating process is based on the carbon saturation of a transition metal upon exposure to a hydrocarbon gas at high temperatures. Subsequently, when the substrate cools down, the solubility of carbon in the transition metal decreases and a thin carbon film precipitates from the substrate surface.

### 2.2.0.2 Properties of graphene

The following properties are just a short outline of all the characteristics this material exhibits referring to electrical, thermal and mechanical properties.

Due to its two-dimensional crystal structure, graphene shows a high electron mobility (100 times faster than in silicon). This high electron mobility and high electrical conductivity is based on the fact that carbon has a total of 6 electrons (2 in the inner shell and 4 electrons that bond). In a two-dimensional crystal such as graphene, every carbon atom is bonded with 3 other carbon atoms, which means that one electron remains free for conducting electricity. Furthermore, graphene is applied in integrated circuits with increasing device density to handle the thermal management - the thermal conductivity of graphene is in a range of 2000-4000 W/m K (copper: 400 W/m K) [9].

Single-layer graphene usually shows a high symmetry of its honeycomb-like structure, but without having a band gap, in contrast to the more versatile bilayer graphene, for which a transverse electric field can open a gap and strain can qualitatively change the low-energy band structure. Hence the usage of graphene in semiconductor industry is far-reaching [10]. Further graphene stands out through its mechanical characteristics such as ultimate strength values based on its  $sp^2$  hybridisation ( $\pi$  bonds) that are 1000 times higher compared to A36 structural steel.

On the other hand, the Young's modulus of graphene is very high (around 1 TPa) which might be detrimental for applications described in this work.

## 2.3 Processing

### 2.3.1 Paste material and wafer stack

Basically, the pastes which were used for the printing processes described in this thesis consist of copper particles (micro-nano or nano sized particles), capping agents which hinder the copper particles to agglomerate and solvents to control the viscosity of the paste and ensure a suitable printing behaviour.

The wafers which were used as basic stack for all of the following experiments consist of 725 $\mu$ m Si/150nm TiW/150nm Cu seedlayer. The thin TiW-layer directly on the Si-substrate acts as a barrier stopping the diffusion of copper particles into the silicon basic material. The thin copper (seed-)layer ensures adhesion of the printed copper layer to the stack.

### 2.3.2 Printing

As already mentioned shortly in chapter 1 one characteristic advantage of printed copper refers to a small time-deposition ratio. Basically there are two different ways of printing pasty materials already used in semiconductor industry, for example the deposition of solder paste by stencil printing. All of the results described in chapter 3 were printed by stencil printing methods. Hence the following paragraphs describe the principle of stencil printing. As can be seen in fig 2.4, viscous material that should be printed on the substrate is distributed over a thin metallic foil with holes of specific dimensions. Moving squeegees force the paste to fill the gaps by rolling it in the moving direction (see fig 2.4). To reach satisfying paste distributions, materials with thixotropic characteristics are required.

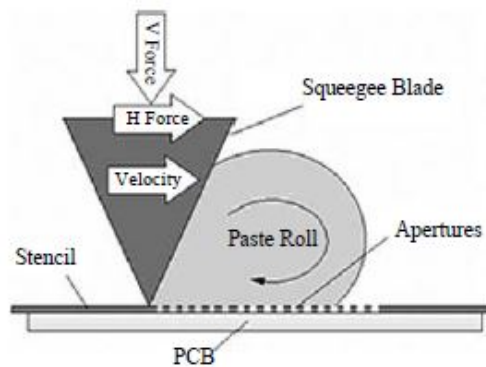


Figure 2.4: Outline of paste movement during printing process. Source: [11]

The stencil printing process is schemed in fig 2.5. As can be seen in subfigure (a), first the stencil is placed on the wafer by aligning the stencil fiducials with the wafer fiducials. Subsequently, the paste is deposited into the free spaces of the screen by a moving squeegee, subfigure (b). The lowest subfigure, (c), shows the printed paste after removing the stencil.

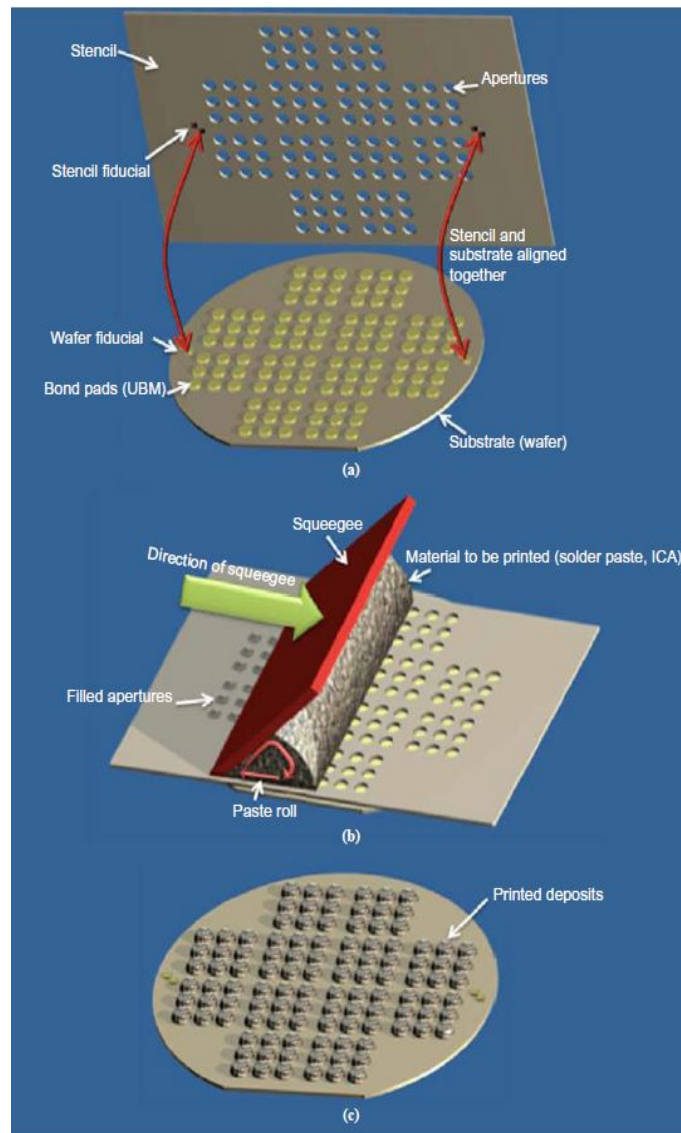


Figure 2.5: Schematic overview of the stencil printing technique. [11]

Several parameters should be optimized to achieve satisfying printing results. Obviously, these parameters vary mainly depending on the viscosity of the used paste. Even though the use of standardized parameters for different pastes entails that the printing process cannot be optimized for all of them, all pastes were printed with the same parameters (listed in table 2.1) to achieve comparable results, e.g. concerning the deposited thickness.

Table 2.1: Generally used printing parameters

Parameter	Value
Stencil Thickness	50 $\mu\text{m}$
Board Thickness	3.8 mm
Front Print Speed	5.0 mm/s
Rear Print Speed	5.0 mm/s
Separation Speed	1.0 mm/s
Separation Distance	3.0 mm
Front Pressure	9.0 kg
Rear Pressure	9.0 kg

The printing was done under clean room conditions by use of a DEK Horizon industrial printer manufactured by *DEK Printing Machines Ltd.* For industrial printing processes it is meaningful to use a combination of a printing and a wafer handling tool to achieve a standardized metal deposition. Both tools are shown in fig. 2.6.



Figure 2.6: DEK printer assembly. Source: [12]

### 2.3.3 Drying

The drying step of the deposited paste should be as controlled as possible. Therefore the wafers were dried immediately after printing. The main reasons for requiring a separate drying step firstly lies in a safer and simplified wafer handling and transport out of the clean room and secondly in an additional and more detailed information about this process step. Further informations can always be helpful to reconsider every impact and effect occuring

during processing, especially if the printed layers do not follow expected behaviour. All drying processes were done using the furnace shown in fig. 2.7.



Figure 2.7: View on the insight of the *YES* furnace

As already mentioned, the drying step was done directly after printing and weighing of each wafer. Therefore all wafers were put into one of the furnace's four chambers by use of a wafer carrier. Previous experiments had shown that differences in the use of various chambers do not lead to a relevant deviation in some investigated output parameters. According to manufacturer information, the whole solvent content evaporates between 60-100 °C. Hence the wafers stay in the furnace for around 30 minutes at a holding temperature of 100 °C and nitrogen atmosphere.

### 2.3.4 Curing

Curing represents the last process step. The used furnace which is shown in fig. 2.8 is fabricated by *ATV Technology GmbH*. The Furnace consists of a furnace chamber, a cooling system and a rough vacuum pump which reaches pressure levels around 3 mbar. The wafer is heated up via a heating plate for which the temperature is controlled by two thermocouples directly attached to the plate.

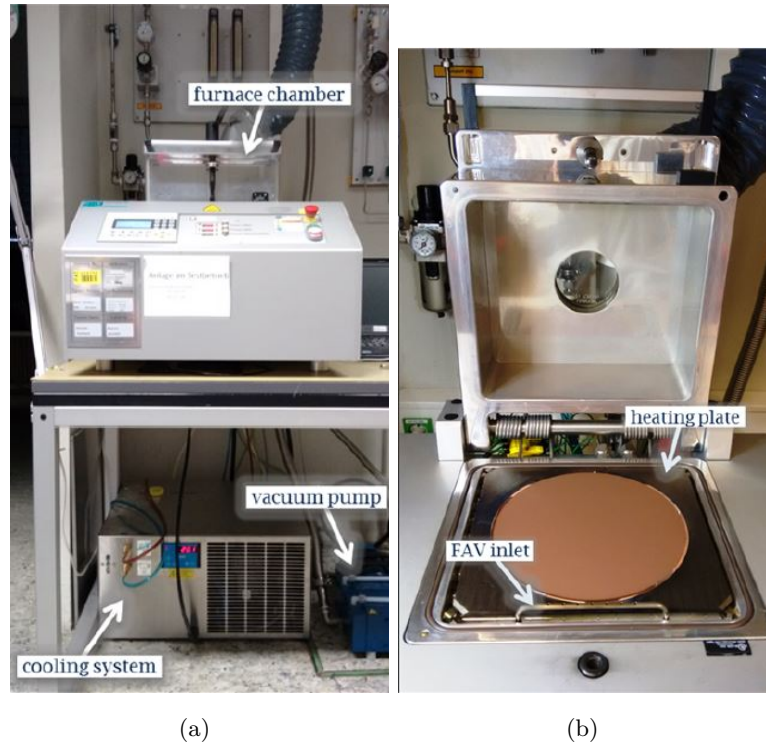
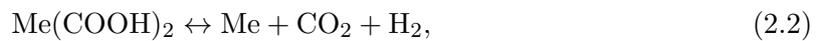


Figure 2.8: (a) ATV furnace with vacuum pump and cooling system. (b) Furnace chamber. Source: [13]

In general, copper oxidizes very quickly at higher temperatures. Therefore a combination of an inert carrier gas and a reducing agent is required to achieve conducting and purified copper structures. Hence, after heating the wafer up to temperatures above  $100\text{ }^{\circ}\text{C}$ , a mixture of  $N_2$  and *formic acid* ( $HCOOH$ ) is led into the furnace chamber. Further on, this mixture is called *formic acid vapor* (FAV). At temperatures higher than  $200\text{ }^{\circ}\text{C}$ , following reactions 2.2 and 2.3 are triggered [14],



Additionally, the use of formic acid vapour is required to reduce the content of organics in the pastes.[13]

To provide equal starting conditions for all cured wafers the chamber has to be cleaned with *isopropyl alcohol* ( $C_3H_8O$ ) after each curing process to completely remove products that were formed due to decomposed organic components of the used pastes. Afterwards the isopropyl alcohol residues can be evaporated and extracted by heating the chamber up to around  $90\text{ }^{\circ}\text{C}$  under vacuum and subsequently flushing with  $N_2$  atmosphere.

All programs that were used to sinter the different pastes are based on previous experiments done by *B. Eichinger* with *Infineon Technologies Austria AG* [13]. Samples that will be compared afterwards were always heated up to 400 °C using the same ramp rate and a temperature plateau at 100 °C. The curing processes mainly differ in 400 °C holding times that equal 0, 60 and 180 minutes. The detailed process flows are shown in fig. 2.10 - 2.12 and shortly described in tab. 2.3 - 2.5. In the following, these processes will be abbreviated as 400-000, 400-060 and 400-180 with respect to the holding temperature and the holding times.

Fig. 2.9 shows the main process steps which are used for all curing processes with a maximum temperature of 400 °C. The steps are explained subsequently in tab. 2.2.

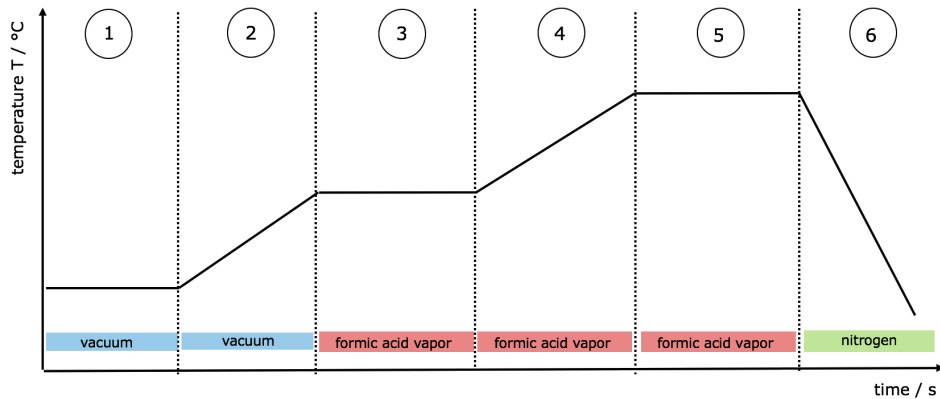


Figure 2.9: Main steps of a process using 400 °C as maximum temperature.

Table 2.2: Description of the main steps during a curing process.

Step	Action	Atmosphere	End temperature / °C	Treatment step
1	evacuating	air → vacuum	RT	inertization
2	heating up	vacuum	100	pretreatment
3	holding	FAV	100	reduction
4	heating up	FAV	400	sintering
5	holding	FAV	400	annealing
6	cooling	nitrogen	RT	-

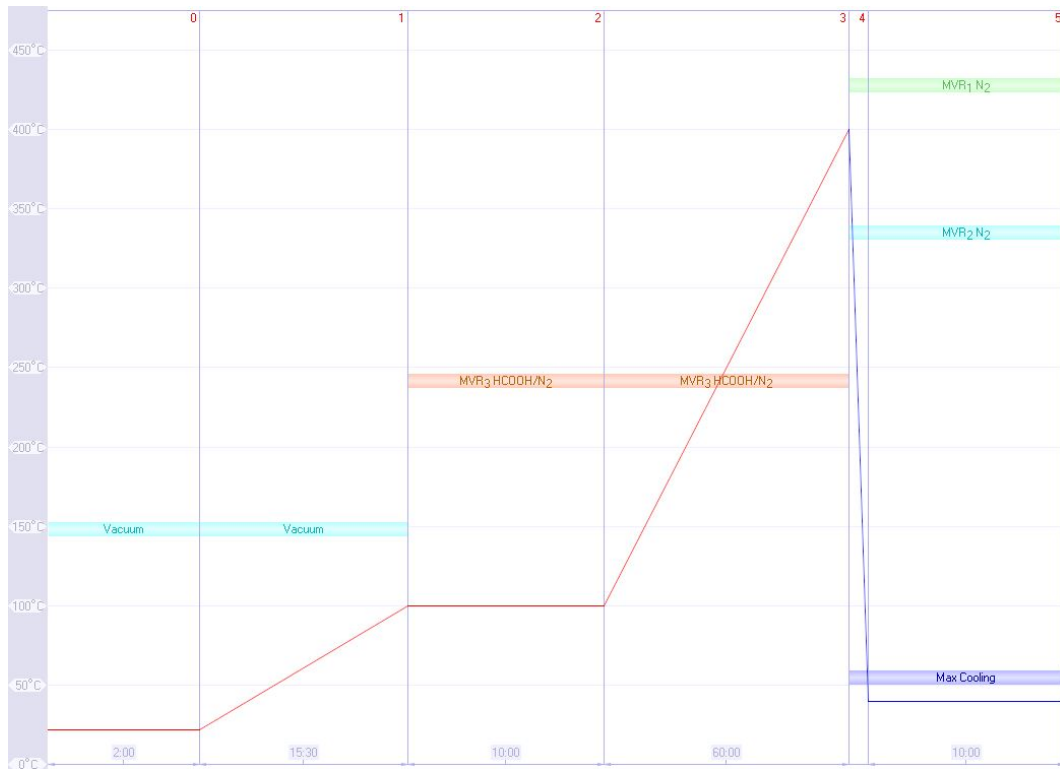


Figure 2.10: Process flow of the recipe: 400-000

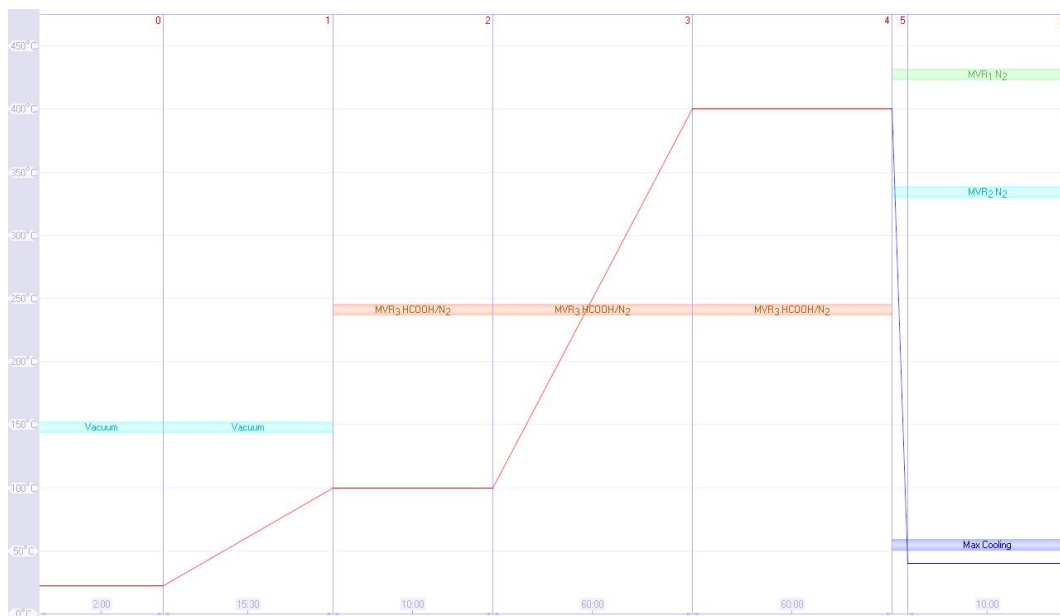


Figure 2.11: Process flow of the recipe: 400-060

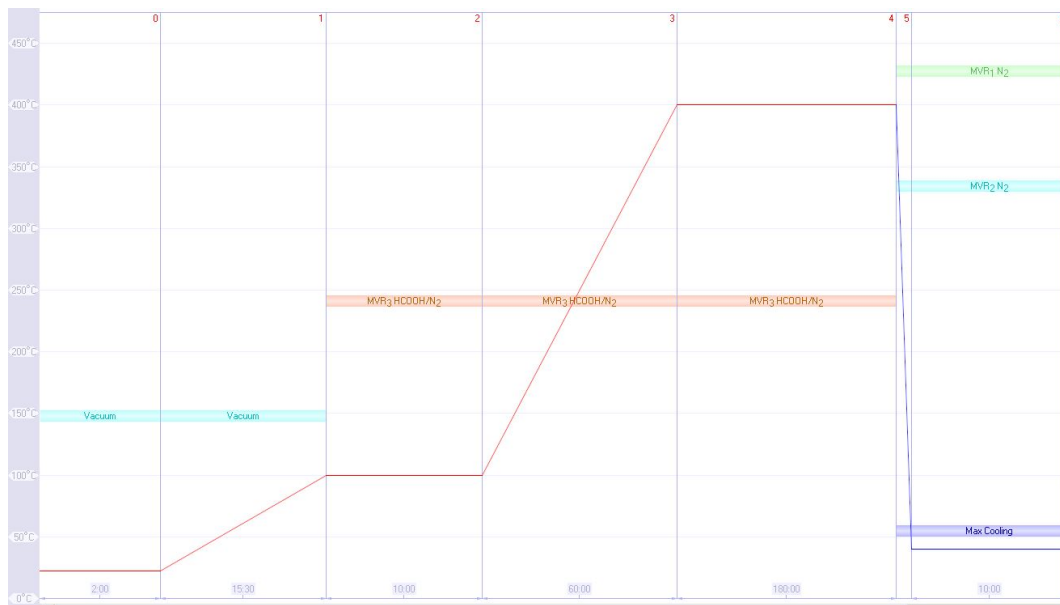


Figure 2.12: Process flow of the recipe: 400-180

Table 2.3: Description of curing process: 400-000

Step	Action	End temperature / °C	Ramp rate / (°C/min)	Step time / min	Atmosphere
0	evacuating	RT	0	2.0	air → vacuum
1	heating up	100	5	15.5	vacuum
2	holding	100	0	10.0	FAV
3	heating up	400	5	60.0	FAV
4-5	cooling	RT	na	10.0	nitrogen

Table 2.4: Description of curing process: 400-060

Step	Action	End temperature / °C	Ramp rate / (°C/min)	Step time / min	Atmosphere
0	evacuating	RT	0	2,0	air → vacuum
1	heating up	100	5	15,5	vacuum
2	holding	100	0	10,0	FAV
3	heating up	400	5	60,0	FAV
4	holding	400	0	60,0	FAV
5-6	cooling	RT	na	10,0	nitrogen

Table 2.5: Description of curing process: 400-180

Step	Action	End temperature / °C	Ramp rate / (°C/min)	Step time / min	Atmosphere
0	evacuating	RT	0	2,0	air → vacuum
1	heating up	100	5	15,5	vacuum
2	holding	100	0	10,0	FAV
3	heating up	400	5	60,0	FAV
4	holding	400	0	180,0	FAV
5-6	cooling	RT	na	10,0	nitrogen

## 2.4 Characterization Methods

### 2.4.1 Standardized characterization

Due to error estimation and minimization issues it is meaningful to undergo a standardized characterization sequence to ensure comparability of the results. Hence all processed samples have been characterized using the same sample preparation and tools. Each wafer was broken into 6 samples from different wafer regions (see fig. 2.13).

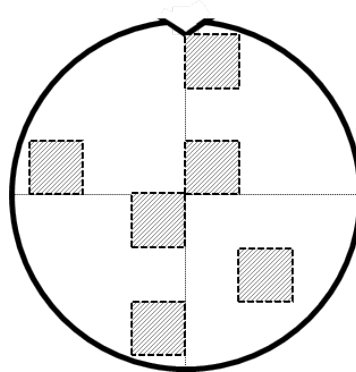


Figure 2.13: Positions of samples used for standardized characterization.

#### 2.4.1.1 Solids content

To determine and compare the paste's solid content to the data stated by the external supplier, the mass of the solvent has to be subtracted of the total paste mass. Therefore, the wafers are weighed before printing and after printing to know the exact amount of paste deposited on the wafer. Additionally, printing parameter can be controlled and adjusted namely by checking if the deposited amount of paste fits the expected values. In order to determine the solid content, the wafers are also weighed after the drying step. At 100 °C, solvents should evaporate totally and merely metal particles and organic coatings should remain. So weighing after drying leads to the percentage of weight that indicates the solid content.

Hence, provided that the total amount of solvent contained in the printed layer evaporates

during the drying step, the percentage of solid  $s$  can be approximately calculated by using eq. (2.4),

$$s = \frac{100}{m_w} m_d \quad (2.4)$$

with the weighed mass of the wet paste  $m_w$  and the mass of the paste after drying at 100°C  $m_d$ .

### 2.4.1.2 Specific Resistivity

The determination of the layer's specific resistivity is another task of the basic characterization. Given the validity of the Wiedemann-Franz law for porous metals, knowledge about the specific electrical resistivity can be used directly as an indicator for heat conductivity values.

#### 2.4.1.2.1 Electrical and thermal conductivity in metals

Basically the *electrical conductivity*  $\sigma_{el}$  of an isotropic solid is defined as the product of the charge carrier concentration  $n$ , the elementary charge  $e$  and the charge carrier mobility  $\mu$

$$\sigma_{el} = n \cdot e \cdot \mu . \quad (2.5)$$

Regarding the charge carrier mobility, electrons are accelerated depending on the applied electrical field, which would theoretically, concerning an ideal crystal structure, lead to a steady increase of the electrical current with time. Due to scattering effects of the electrons with other electrons, phonons, structure defects or interfaces, the electrical current reaches a constant value directly after applying an electrical field. Additionally, the electrical field itself and gradients of the temperature or the chemical potential have an impact on the movement of the electrons. All these dependencies are considered using the so-called *drift velocity*  $v_D$  which indicates the mean velocity of moving electrons. Under the assumption of  $v_D = const.$  the charge carrier mobility is given by

$$\mu = \frac{e\tau}{m_e} . \quad (2.6)$$

Further, the electrical conductivity is given by

$$\sigma_{el} = \frac{ne^2\tau}{m_e} \quad (2.7)$$

with  $\tau$  the mean time between two consecutive scattering processes and  $m_e$  and  $e$  the mass and the charge of an electron ([15],[16]). It is measured in units of  $S\ m^{-1}$  or  $\Omega^{-1}\ m^{-1}$ .

The reciprocal value of the electrical conductivity equals the *electrical resistivity*  $\rho_{el}$

$$\rho_{el} = \frac{1}{\sigma_{el}}, \quad (2.8)$$

which is measured in units of  $\Omega \text{ m}$ .

Both the transport of electrical and thermal energy in metals is through conduction of electrons. Hence the electronic contribution of the thermal conductivity ( $\lambda$ ) is proportional to the electrical conductivity ( $\sigma$ ) [17]. This correlation is shown by Wiedemann-Franz-law,

$$\frac{\lambda}{\sigma} = L \cdot T \quad (2.9)$$

with the Lorenz number  $L$  and the temperature  $T$ .

Since the fluctuation of the Lorenz number of copper is low for a temperature range from around 300 - 1000°C, the measured electrical resistivities of different copper layers can be used as comparable values for evaluation of the layer's general performance at RT and higher temperatures [18].

#### 2.4.1.2.2 Four-point probe method

The sheet resistivity of the printed layers was determined using the so-called *Resmap168* tool fabricated by *Creative Design Engineering, Inc.* which is based on the principle of a four-point probe measurement.

The basics about the setup of this method are sketched in fig. 2.14.

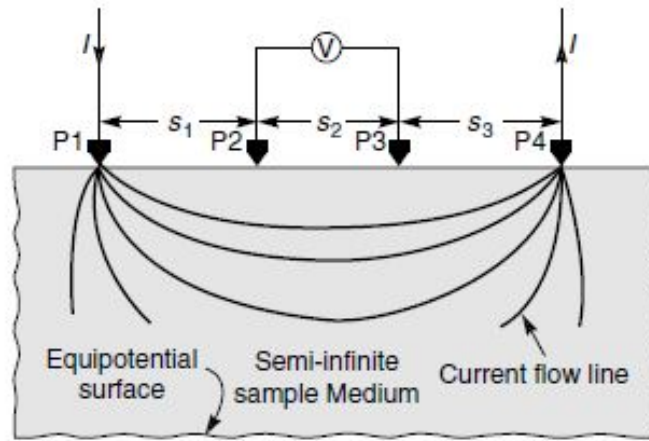


Figure 2.14: Four-point probe measurement. Source: [19]

P1-P4 indicate four sharp probes that are mechanically pressed onto the testing sample surface. A constant current is applied through the two outer probes (P1 and P4) which leads to a measurable voltage drop across the two inner probes (P2 and P3).

Consequently the specific resistivity is given by eq. (2.10) in units of  $\Omega$  or rather  $\Omega_{\square}$ .

$$\rho_{el} = \frac{2\pi \frac{V}{I}}{\frac{1}{s_1} + \frac{1}{s_3} - \frac{1}{s_1+s_2} - \frac{1}{s_2+s_3}} \quad (2.10)$$

Here,  $V$  is the voltage,  $I$  the current and  $s_1$ ,  $s_2$ ,  $s_3$  and  $s_4$  are the probe spacings [20].

To obtain reliable results, the distance between two probes has to be equal.

Subsequently, the specific resistivity of the layer can be calculated by multiplying the sheet resistivity values with the layer thickness.

### 2.4.1.3 Layer Thickness

The determination of the layer thickness plays an important role to evaluate the general performance of the paste, since the fast and cheap deposition of thick layers is one of the main advantages of using pastes for wafer metallization. Therefore, a certain thickness of the sintered layer has to be expected.

Furthermore, the layer thickness is required to calculate the specific resistivity.

#### 2.4.1.3.1 Scanning probe microscopy - Profilometer

The measurements regarding layer thicknesses were done using a *BRUKER DektakXT* stylus profiler. The mode of operation is based on a tip which is mechanically scanning across the sample's surface and recording the peaks and valleys. In this way the surface roughness as well as the layer thickness can be determined. The measurement accuracy mainly depends on the scanning time and the tip size. The used profilometer had a tip radius of  $r = 2 \mu m$ . The scanning process is sketched by fig. 2.15.

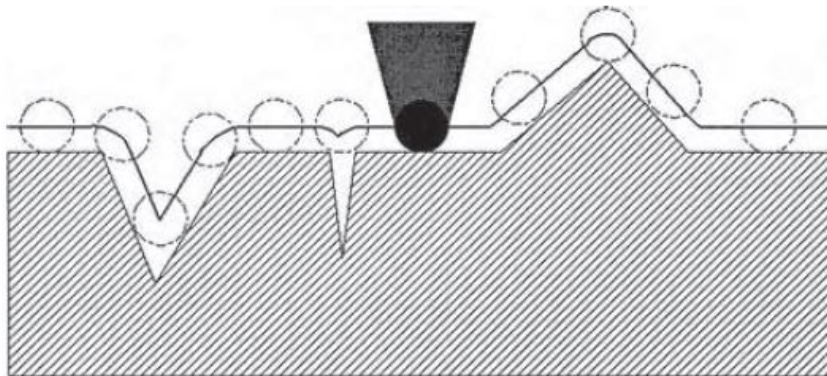


Figure 2.15: Mechanical profilometer. Source: [21]

#### 2.4.1.3.2 Sample preparation for layer thickness measurements

Due to the fact that all of the used samples were pieces of wafers which had been printed unstructured it was inevitable to condition these samples before measuring. Hence, in order

to provide a height step that is required for measuring the layer thickness, the copper was etched partially as shown in fig. 2.16.

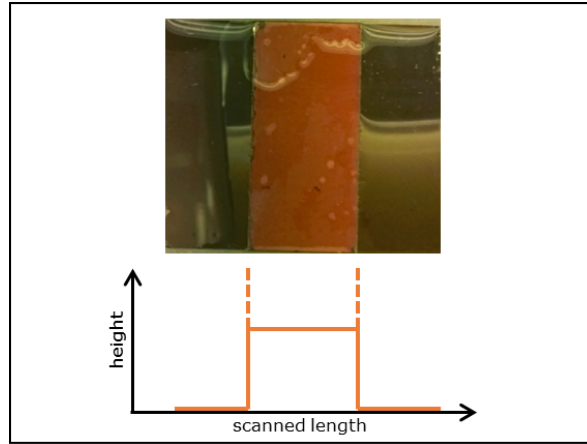
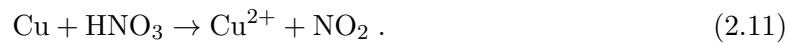


Figure 2.16: Etching pattern and scheme of expected corresponding height profile.

Since copper dissolves by reacting with concentrated nitric acid (69 %  $\text{HNO}_3$ ) this acid was used to partially remove the copper layer and provide a height step. The nitric acid is only etching the copper metallization, not the silicon substrate.

The general chemical reaction reads as follows [22],



Regarding, in addition, the load and mass balance, following reaction occurs,



#### 2.4.1.4 Porosity

Most of the physical properties (e.g. electrical resistivity and Young's modulus) correlate with the porosity of the material.

Various methods exist to determine the layer's porosity. In this case the porosity was determined by use of the so-called Archimedes method. Therefore the sample was weighed once as the entire area of the sample was covered by copper and again after dissolving of the entire copper layer (additional etching step). Using this weight difference and the layer's volume it is possible to calculate the density of the porous copper layer. The ratio between the porous

copper's ( $\rho_p$ ) and the bulk copper's ( $\rho_{Cu} = 8.92 \text{ g/cm}^3$ ) densities equals the porosity ( $P$ ) of the printed copper layer,

$$P = 100 - \frac{\rho_p}{\rho_{Cu}} \cdot 100 . \quad (2.13)$$

The volume of the copper seed layer is already considered by calculating the volume of the porous copper layer.

Calculations show that in the case of the used copper-graphene composite layers the contribution of the graphene can be neglected for porosity calculations.

The Archimedes method is a very fast method, but the determined values depend on the accuracy of the height and volume measurement.

#### 2.4.2 Scanning Electron Microscopy

To get information about the paste's microstructure, a scanning electron microscope (SEM) was used. Depending on the resolution of the microscope different effects on the surface can be made visible by scanning across the surface, e. g. topography, material contrast and crystal structure. Theoretically, the highest resolution is about the size of one single atom, i.e. 1 Å. The principle of a SEM is shown in fig. 2.17.

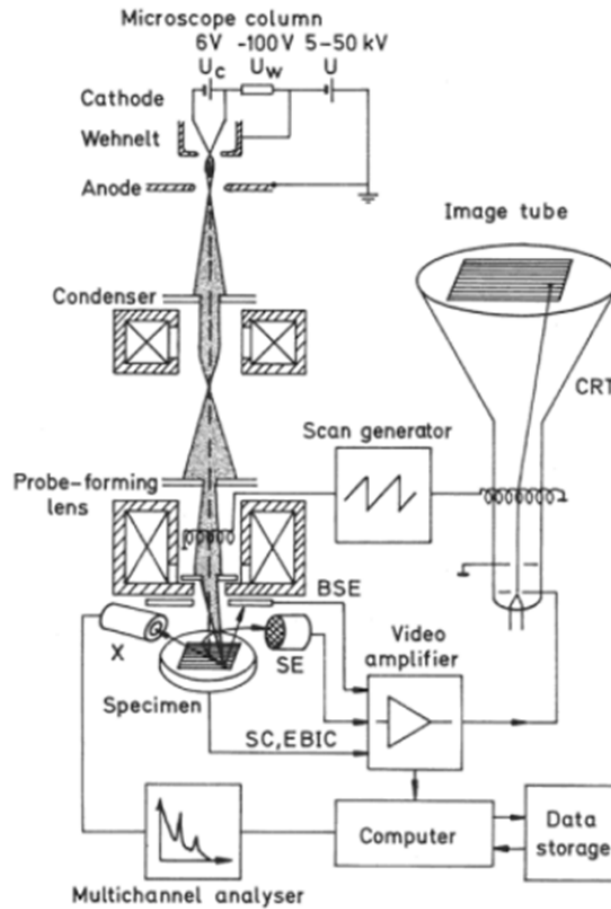


Figure 2.17: Principle of a scanning electron microscope. Source: [23]

The electron gun (cathode, Wehnelt cylinder and anode) generates electrons that are focused by a magnetic lens system before interacting with the sample's surface. The probe-forming lens and the coils are necessary to scan different regions of the sample. The interaction possibilities of electron beam and sample depend on the sample material as well as on the operating voltage and are shown in fig. 2.18. Two types of interaction possibilities, i.e. secondary electrons (SE) and back scattered electrons (BSE) are shown in fig. 2.17. The detection of secondary and back scattered electrons is different. To detect secondary electrons, usually an Everhart-Thornley-detector is used. Back scattered electrons can be detected by a Robinson-detector, which is similar to an Everhart-Thornley-detector. Further also solid state detectors or in-lens detectors can be used to detect BSE. [23]

Detector  $x$ , shown in fig. 2.17, is used for energy dispersive x-ray spectroscopy which will be described in ch. 2.4.2.1 .

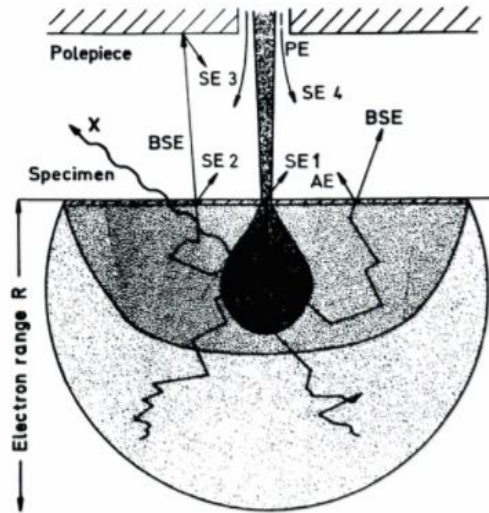


Figure 2.18: Scanning electron microscope - interaction volume. Source: [24]

The different electron types shown in fig. 2.18, i.e. back scattered electrons (BSE), different groups of secondary electrons (SE1-SE4), Auger electrons (AE) and primary electrons (PE) are detected by separate detectors.

#### 2.4.2.1 Energy dispersive x-ray spectroscopy

Scanning electron microscopes can further be used to generate information about the chemical composition of a sample. This application of the SEM equals x-ray spectroscopy which can be based on wavelength- or energy-dispersive x-rays. For the following investigations, exclusively energy-dispersive x-ray spectroscopy was used.

Due to electrons which are accelerated onto the samples surface and to the subsequent collision electrons of the sample material are knocked out from inner atomic shells. Missing electrons are instantaneously replaced by nearby electron from the next shell. This jumping electron simultaneously emits the excessive energy as an x-ray photon. This type of emission is called characteristic x-ray radiation and can be measured by semiconductor detectors. Since characteristic x-ray radiation is available for all elements from the periodic table, it is possible to determine the chemical composition of the investigated sample [25].

#### 2.4.3 Focused Ion Beam

Investigating the cross sections of samples exclusively using a SEM causes problems regarding getting a focused image, due to the high roughness of the cross section of a manually broken sample under investigation. To prevent such difficulties a so-called FIB (Focused Ion Beam) can be used. Very often SEM and FIB applications are combined.

Generally, there are four functionality types of a FIB including milling, deposition, imaging

and implantation with high energy ions. Basically, the FIB instrument consists of a vacuum system and chamber, a liquid metal ion source, an ion column, a sample stage, detectors, gas delivery system and a computer to run the complete instrument. The principle is very similar to the functionality of a SEM. Instead of electrons, a FIB is based on ions (mainly gallium or helium) interacting with the surface [27].

The principle of a dual-beam FIB-SEM instrument can be seen in fig. 2.19 [26]. The electron as well as the ion ( $\text{Ga}^+$ ) column is shown in fig. 2.19. Additionally, on the left side of fig. 2.19, the interaction of electrons and ions with the solid sample is schemed.

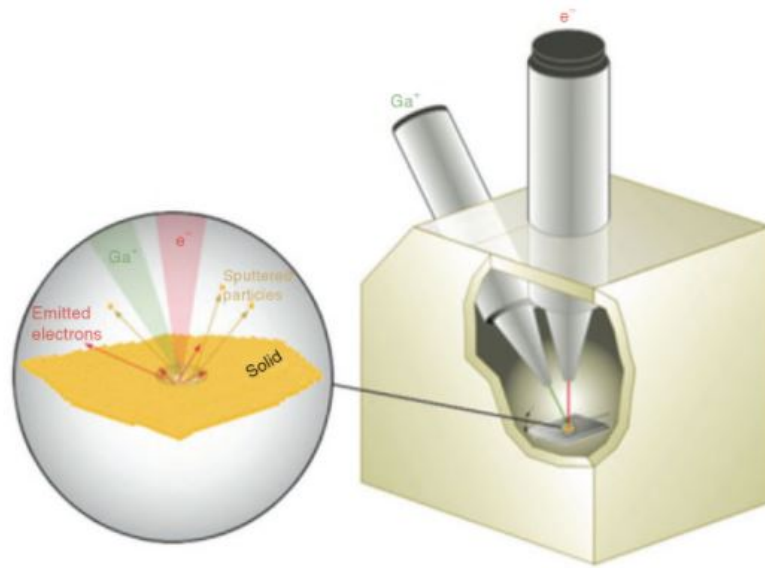


Figure 2.19: Principle of a dual-beam FIB-SEM instrument. Source: [26]

Concerning this work, FIB investigations were done to cut a smooth cone into the copper layer. Hence it was possible to get an focused image by tilting the sample and focus on the smooth cross section.

#### 2.4.4 Thermomechanical Analysis

Thermomechanical Analysis (TMA) is a popular characterization method in materials science to determine, among others, the coefficient of thermal expansion (CTE) of a sample. The principle is based on deformation and dimensional changes due to mechanical loading and heat. Generally, there are four operating types of thermomechanical analysis including compression, tension, penetration and flexure mode [28].

The principle of a TMA is sketched in fig. 2.20.

Fig. 2.20 shows a sample which is heated by a furnace and deformed by a stamp which is under load.

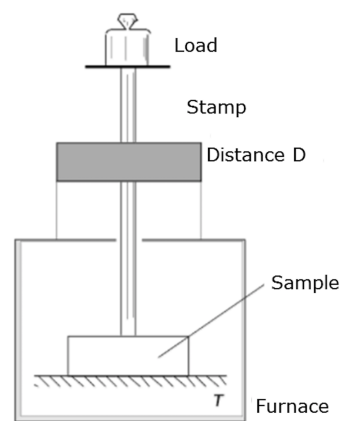


Figure 2.20: Principle of a thermomechanical analysis. Source: [29]

The results shown in ch 3 were investigated by thermomechanical analysis using compression mode.

#### 2.4.5 Dynamic Mechanical Analysis

Another important characteristic of the investigated samples is Young's modulus. It describes the stress-strain behaviour of the material in the elastic region. The determination of Young's modulus can be done investigating the sample by use of dynamic mechanical analysis (DMA). The functionality of a DMA is based on an applied oscillating force (sinusoidal stress) and recording the material's response (deformation or strain) to that force. Fig. 2.21 sketches the principle of a dynamic mechanical analysis.

As can be seen in fig. 2.21 the force motor is connected to a drive shaft which transfers a sinusoidal force (stress) on the sample which results in a sinusoidal deformation of the sample (strain). On the right side of fig. 2.21 the sine wave generated by the force motor and the sine wave detected by a linear variable differential transformer (LVDT) are shown. Using these curves, the storage ( $E$ ) and loss ( $E'$ ) modulus can be determined. The storage modulus  $E$  can be used to describe the Young's modulus. The vibration energy is indicated by the loss modulus ( $E'$ ). The dissipation factor ( $\tan \delta$ ) equals the ratio of  $E'$  and  $E$  and describes the mechanical damping.

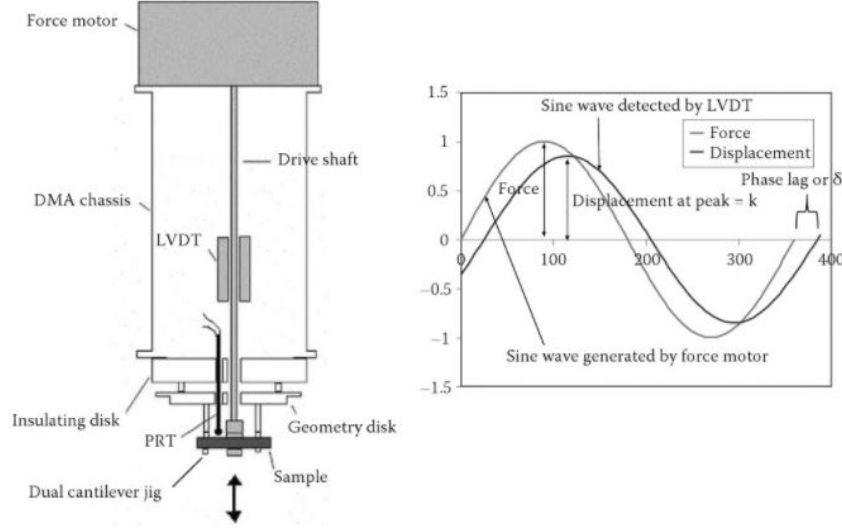


Figure 2.21: Principle of a dynamic mechanical analysis. Source: [30]

The results concerning TMA and DMA were provided by *H. Preu, Infineon Technologies AG*.

#### 2.4.6 Wafer bow measurements

To measure the wafer bow of a sample during heating and cooling, a measurement method developed and operated by *M. Schneegans, Infineon Technologies AG* was used. The measurement is based on a laser beam being split into an array of laser points which are projected onto a reflecting sample surface. Due to a mismatch in the CTEs between the copper layers and the Si-substrate a wafer curvature is induced during heating. The different expanding rates of the materials cause a bow of the sample and a distance variation of the reflected laser points. Using the displacement of the reflected laser points, the increase and decrease of the wafer bow can be calculated.

To calculate the stress  $\sigma$  in a sample from the measured bow data, Stoney's equation (eq. (2.14)) can be used. It is important to note that this equation is valid only for dense material and therefore cannot simply be used in order to calculate the stress in a porous material. Instead of calculating absolute stress levels, it is nevertheless possible to calculate the difference between the minimum and maximum stress of a porous sample, which can be compared to the value of the bulk material to get a rough estimate for the stress level.

$$\sigma = \frac{Et_s^2}{(1-\nu)6t_f} \left( \frac{1}{R_2} - \frac{1}{R_1} \right) \quad (2.14)$$

whereas  $E$  is Young's modulus,  $\nu$  is Poisson's coefficient,  $t_s$  and  $t_f$  are the thickness of the substrate and the film, respectively, and  $R_1$  and  $R_2$  are the radii of the substrate before and after deposition of the thin film [31].

### 2.4.7 Raman spectroscopy

Raman spectroscopy embraces the characteristic periodic motions of atoms that are connected by elastic bonds. Formally, all of these motions of atoms relative to each other are a superposition of so-called normal vibrations whereby the different vibrational degrees of freedom can be described. The number of normal vibrations for polyatomic molecules with  $n$  atoms equals the result of  $3n - 6$  and  $3n - 5$  for linear molecules. Hence, vibrational spectra typical for certain molecules are defined depending on their atomic masses, geometrical arrangement and chemical bonding strength [32].

Raman spectroscopy is further based on the interaction of light and matter and the subsequent impact processes. This is due to the fact that Raman scattering describes an inelastic scattering process which causes a change in the energy of the light quantum characteristic for each element. The frequency of the scattered light is independent of the direction of scattering and differs from the excitation frequency by the amount of the so-called Raman shift  $\Delta\nu$ , which is described by eq. (2.15) [33].

$$\Delta\nu = \frac{(E_n - E_k)}{h} \quad (2.15)$$

with the energy state after the scattering process  $E_n$ , the energy state before the scattering process  $E_k$  and  $h$ , Planck's constant.

Raman spectroscopy can be used in different fields of application. In this work, Raman analysis was used for stress determination in the silicon substrate (chapter 2.4.7.1) as well as for classification and determination of graphene qualities in the porous copper-graphene layer (chapter 2.4.7.2). All measurements concerning Raman spectroscopy were done in cooperation with *Carinthian Tech Research AG*.

#### 2.4.7.1 Determination of stress states in the silicon substrate

Stress in the silicon substrate can be easily induced by manufacturing processes, such as thinning of the wafers or chip separation. Raman spectroscopy is a non-destructive method to determine the stress which is a considerable advantage in application [34]. Unstrained silicon has three degenerated Raman modes including two transverse optical modes and one longitudinal mode, which all depend on the polarization and have the same frequency of  $520.5 \text{ cm}^{-1}$ . Compressive stress and tensile strain induce different shifts of the center wavelength. Concerning compressive stress, the shift is increasing to a higher center frequency, while tensile strain causes a shift to lower frequencies. It is also possible to calculate the stress state for a silicon wafer with a crystal orientation of (100) analytically [35].

### 2.4.7.2 Classification of graphene

Since graphene shows a characteristic Raman spectrum it is possible to monitor the number of graphene layers and the defect density, which equals the quality of the graphene layers. The Raman spectra of graphite and graphene exactly show this difference in atomic layers, as can be seen in fig. 2.22.

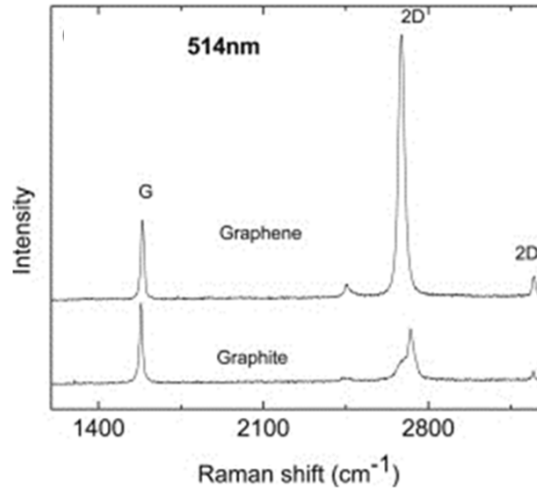


Figure 2.22: Comparison of the Raman spectra of graphene and graphite measured at 514.5 nm. Source: [36]

The two most intense features shown in fig. 2.22 are the G-peak at  $1580\text{ cm}^{-1}$ , and the 2D-peak. The D-peak is not visible in fig. 2.22 but would be at a lower value on the Raman shift scale than the G-peak.

The number of graphene layers depends on the ratio of the 2D- and G-peak. If  $\frac{2D}{G} > 1$  it indicates monolayer graphene. Hence the graphene quality is high and the layer number is low if the spectrum shows a missing D-peak at  $1350\text{ cm}^{-1}$  (indicating small defect density), and an intense and sharp 2D-peak at  $2690\text{ cm}^{-1}$  compared to the G-peak.

## Chapter 3

# Experiments and Evaluation

### 3.1 Characterization of pure copper particle pastes

In a first experimental run five different copper particle pastes were investigated to select one nano particle and one micro-nano particle based paste as base material for the combined copper-graphene pastes. The pastes were provided by an external manufacturer.

All of these pastes were processed and characterized under the same conditions, as described in ch. 2.4.1. The results can be seen in tab. 3.1, micro-nano particle pastes are marked with the suffix *B3* and nano particle pastes with *B2*. The first numbers of the product names are arbitrarily chosen.

Table 3.1: Results of copper particle pastes

product name	layer thickness / $\mu\text{m}$	specific resistivity / $\mu\Omega\text{cm}$	porosity / %
2B3	$7.5 \pm 1.2$	$6.2 \pm 1.1$	$42 \pm 5$
3B3	$8.5 \pm 1.3$	$5.0 \pm 1.0$	$36 \pm 5$
4B3	$18.0 \pm 2.1$	$9.0 \pm 1.1$	$55 \pm 4$
5B2	$4.5 \pm 1.3$	$2.4 \pm 1.1$	$21 \pm 4$
5B3	$25.0 \pm 1.6$	$15.0 \pm 1.1$	$66 \pm 5$

In this context it is experimentally shown that the different theoretical models of the relation between porosity and electrical conductivity (see fig. 2.1) show the same behavior as the results concerning the porous copper pastes (see fig. 3.1). The results shown in fig. 3.1 equal the measured specific resistivity results of the pure copper particle pastes, listed in tab. 3.1, in relation to the measured porosity values of each paste.

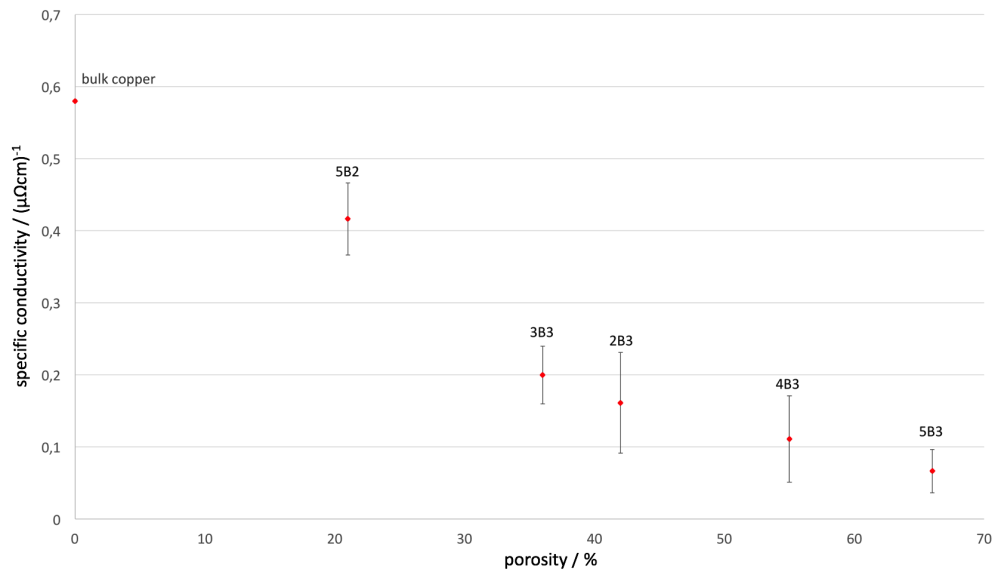


Figure 3.1: Results of copper particle pastes regarding the relation of porosity and resistivity.

Usually by curing, the printed wafers change from a brownish state to pink colored, as can be seen in fig. 3.2. Due to oxidation effects, the surfaces (to the depth of a few nm) of some wafers can be discolored. Tests were done that show that the discoloration effect does not influence the electrical conductivity performance of the wafers. The samples of paste 2B3 and 5B2 show discolored surfaces (see fig. 3.3) after a curing step at 400 °C and holding times of around 180 minutes.



Figure 3.2: Comparison of wafer color after drying (left) and after curing (right).

Source: [13]



Figure 3.3: Surface discoloration effect on samples of paste 2B3 and 5B2 (wafer piece).

Considering the resistivity performance of previous pastes, optimization steps for paste 3B3 and 5B2 had to be done.

The following two pastes are the preferred optimized versions:

- HSB3: micro-nano particles; higher solids content compared to paste 3B3
- 86B2: different nano particles compared to paste 5B2

The results of these two pastes are listed in tab. 3.2. The provided pastes containing graphene are based on these pure copper pastes.

Table 3.2: Results of optimized copper particle pastes

product name	layer thickness / $\mu\text{m}$	specific resistivity / $\mu\Omega\text{cm}$	porosity / %
HSB3	$11.0 \pm 2.8$	$4.0 \pm 0.7$	$33 \pm 8$
86B2	$5.0 \pm 1.2$	$3.1 \pm 1.3$	$25 \pm 5$

## 3.2 Development and characterization of copper-graphene pastes

The aim of combining copper and graphene for wafer metallization is to increase the electrical/thermal conductivity and to model the CTE of the porous metal layer in order to reduce the stress at the silicon/metal interface.

To this end, two different approaches were investigated:

- Mixing of a well-known micro-nano copper particle paste (*CP*) with provided powdery graphene in different qualities and quantities.
- Processing of provided combined copper-graphene pastes.

### 3.2.1 Mixing of copper paste and powdery graphene

The target of the mixing trials was to obtain a porous copper-graphene layer containing a certain amount of graphene after sintering. Thus graphene powder was weighed to achieve

a graphene content of 1 and 5 wt.-%. Subsequently, the graphene powder was dissolved in an ultra-sonic bath using terpineol as solvent. As a last step of preparation the dissolved graphene was manually stirred into the *CP* paste. Two different graphene qualities were used differing from each other regarding the expected final lateral graphene flake size. *Materials grade* graphene is expected to achieve a lateral flake size of around 5  $\mu\text{m}$ . The expected lateral flake size of *premium grade* graphene is between 0.5-1  $\mu\text{m}$ .

The following combinations were mixed (see tab. 3.3).

Table 3.3: Results concerning specific resistivity performance of self-mixed copper-graphene pastes

basic material	graphene content / wt.-%	graphene quality
CP	1	materials grade
CP	1	premium grade
CP	5	materials grade

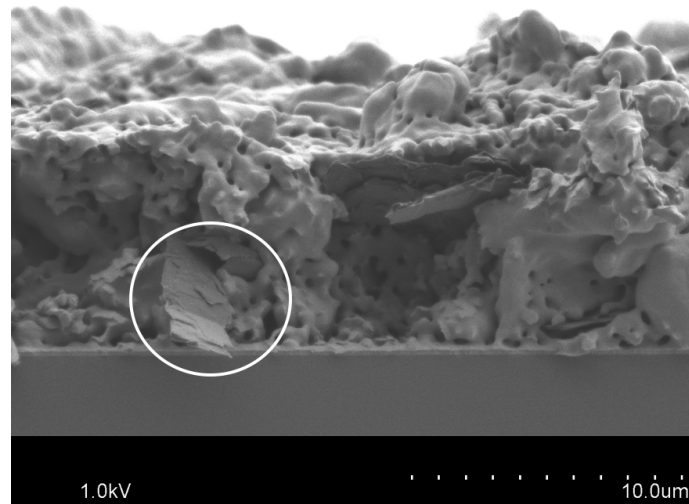
The results of specific resistivity measurements for wafers cured at 400 °C with a temperature holding time of 180 minutes are stated in tab. 3.4.

Table 3.4: Combinations of self-mixed copper-graphene pastes

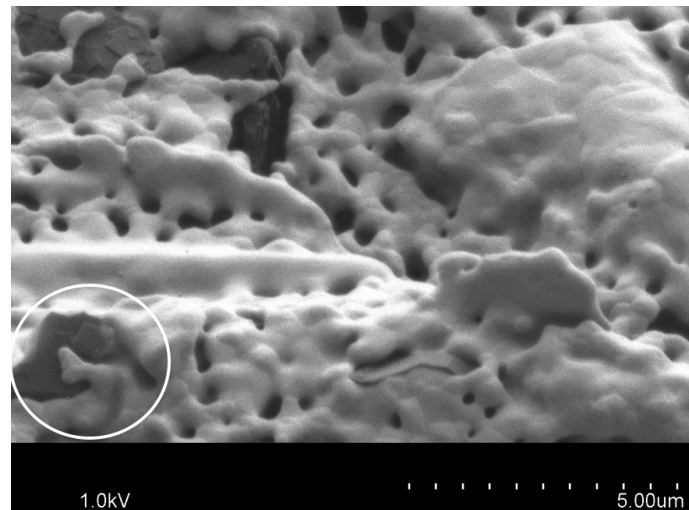
graphene quality	graphene content / wt.-%	average specific resistivity values / $\mu\Omega\text{cm}$
materials grade	1	$5.8 \pm 0.3$
premium grade	1	$5.8 \pm 0.5$
materials grade	5	$8.5 \pm 1.8$

The resistivity values have to be compared with the specific resistivity of the reference paste (CP) without graphene content, which is on average 4.5  $\mu\Omega\text{cm}$  (all reference results are taken from the work of *B. Eichinger, Infineon Technologies Austria AG*). Considering this value the results given in tab. 3.4 show that there is no evident correlation between the graphene specifications and the conductivity performance. On the other hand the content of graphene seems to influence the measured specific resistivity values. Layers with a lower graphene content show a better conductivity performance than the layer with 5 wt.-% of graphene. Further the results show that 1 as well as 5 wt.-% of graphene decrease the conductivity of the metal layer compared to the reference paste.

Fig. 3.4 shows a microscopic image of a sample of the materials grade and 1 wt.-% graphene done using scanning electron microscopy. The graphene flakes visible at the surface as well as on the interface between the metallization layer and the silicon substrate are marked.



(a)



(b)

Figure 3.4: (a) Cross-section of materials grade graphene, 1 wt.-% sample. (b) Top-view of materials grade, 1 wt.-% sample

Further, the stress behavior of these specific samples was investigated using a wafer curvature measurement over temperature. The interpretation of the curve seen in fig. 3.5 is listed in tab. 3.5 and compared to the reference measurement. The measurement consisted of two heating and cooling cycles between 50 °C and 400 °C. They were performed in FAV.

Curve *h1*, shown in fig. 3.5, equals the first heating step of the sample up to 400 °C, followed by the first cooling step down to a temperature of around 50 °C, i.e. curve *cooling 1*. The heating (*h2*) as well as the cooling (*cooling 2*) step is repeated.

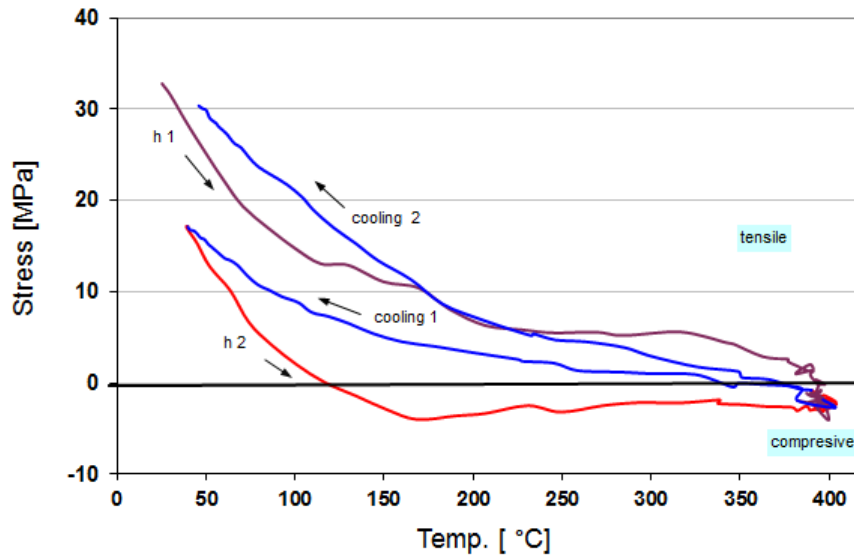


Figure 3.5: Stress behavior of self-mixed paste.

Table 3.5: Combinations of self-mixed copper-graphene pastes

paste	$\sigma_{\min-\max}$ / MPa	$\sigma_{RT}$ / MPa
CP, mat. grade, 1 wt.-%	21	17
CP (reference)	30	23

The stress results listed in tab. 3.5 show that the addition of graphene does not lead to a significant change in the layer's stress behavior.

The graphene spots detected in the above-mentioned sample using Raman spectroscopy show that these samples mainly contain amorphous carbon (dark colored spots) instead of characteristic graphene (mono or multiple layer), as can be seen in fig. 3.6.

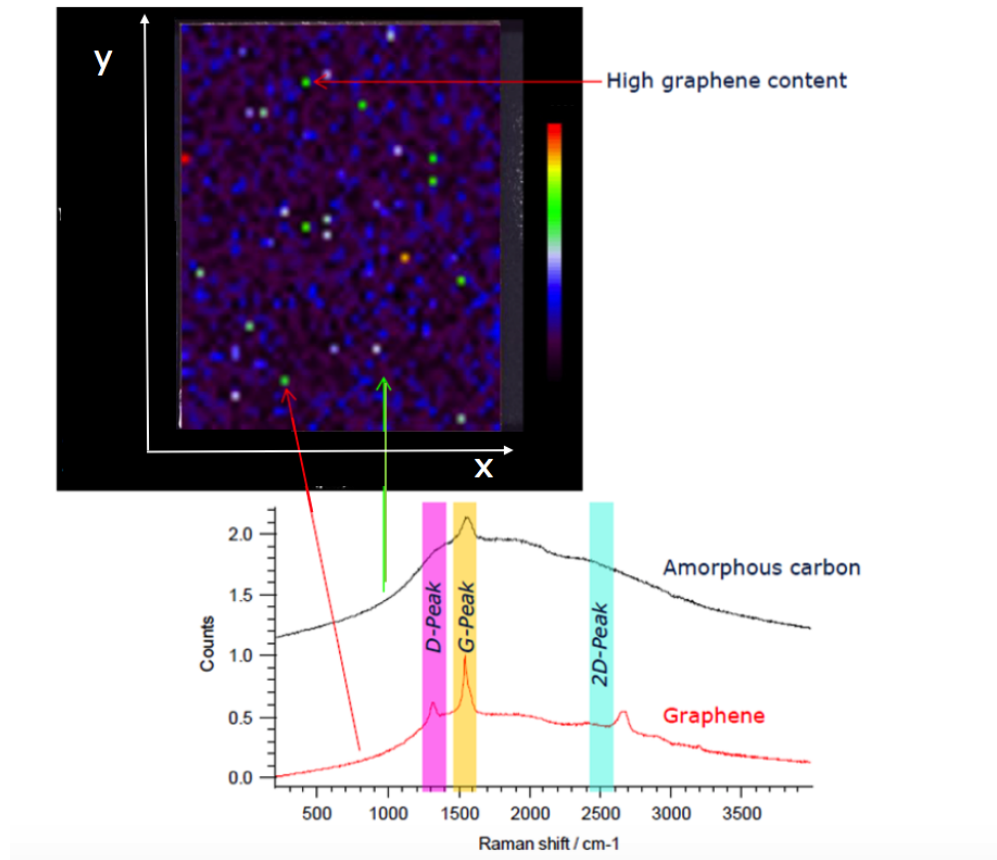


Figure 3.6: Raman spectrum of self-mixed paste.

Due to the fact that the self-mixed pastes showed similar to worse performance concerning graphene quality or resistivity compared to the basic paste without graphene, further optimization steps regarding the graphene content or the curing processes were not performed.

### 3.2.2 Evaluation of provided copper-graphene pastes

In the next two chapters, micro-nano as well as nano copper particle pastes are characterized and evaluated which were printed and processed the same way as the materials described in previous chapters. All of the subsequently described pastes are containing different amounts and qualities of graphene. The specific names are explained in tab. 3.6. To obtain a more convenient overview, the arbitrarily assigned short forms, listed in tab. 3.6 will be used.

Table 3.6: Overview of readily provided pastes

short form	specific paste name	particle size	graphene quality	wt.-% of graphene (marking)
A	B2SL	nano	single layer	0.25 (low)
B	B2SH	nano	single layer	1.00 (high)
C	B2FL	nano	few layer	0.25 (low)
D	B2FH	nano	few layer	1.00 (high)
E	B3SL	micro-nano	single layer	0.16 (low)
F	B3SH	micro-nano	single layer	0.63 (high)
G	B3FL	micro-nano	few layer	0.16 (low)
H	B3FH	micro-nano	few layer	0.63 (high)

### 3.2.2.1 Nano copper particle pastes with graphene content

Same as the previously investigated pastes, pastes *A* to *D* were characterized regarding specific resistivity, CTE, Young's modulus and the respective number of graphene layers. All of the results were compared to the corresponding pure copper paste system, i.e. the nano copper particle paste, which was then used as base material for the combined copper-graphene pastes.

Initially, the specific resistivity of each paste was determined for the cured samples - the results are shown in the boxplots in fig. 3.7 and tab. 3.7.

The horizontal lines inside the boxes equal the median of the data. The lowest and highest, small horizontal, lines outside the boxes equal the minimum and maximum results.

Due to bad printing results of paste *B* caused by a missing thixotropic paste behavior and consequently unreliable measurement values there are no results shown in following box plots. To assess the performance of paste *B* marked value ranges are given in tab. 3.7.

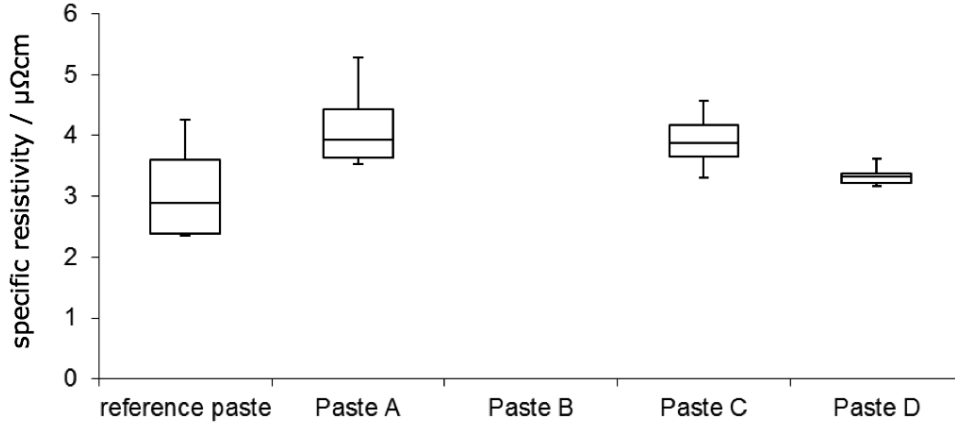


Figure 3.7: Measured specific resistivity data.

Table 3.7: Average specific resistivity values of pastes *A-D* compared to the reference

paste	average specific resistivity value / $\mu\Omega\text{cm}$
reference	$3.1 \pm 1.3$
A	$4.1 \pm 0.7$
B	5-6*
C	$3.9 \pm 0.5$
D	$3.4 \pm 0.4$

Similar to the results of the self-mixed copper-graphene pastes, these pastes have higher specific resistivity values than the reference paste. Again the graphene quality, such as few or single layer graphene or the graphene amount (given that the content is less or equals 1 wt.-%) does not have an essential impact on the conductivity performances.

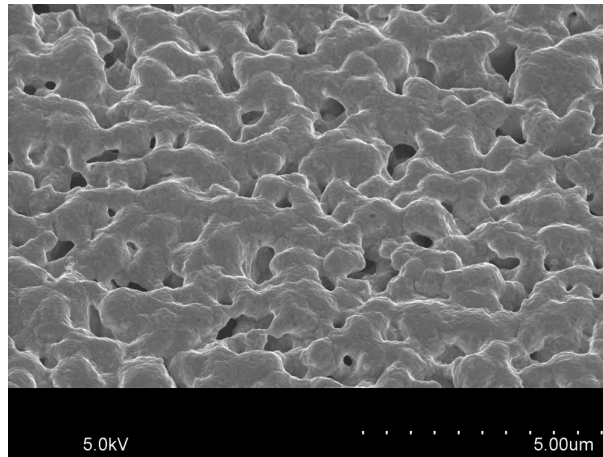
Subsequently all pastes were characterized by a SEM as well as TMA, DMA and Raman spectroscopy. The results of paste *D* are shown in more detail, due to its favorable specific resistivity performance.

Compared to the micro structure of the pure copper paste, the graphene content in the copper-graphene paste is visible as dark agglomerations filling the pores of the surface down to the interface between metallization layer and silicon substrate. The images of the micro structure were done using a SEM. The results can be seen in fig. 3.8 and fig. 3.9.

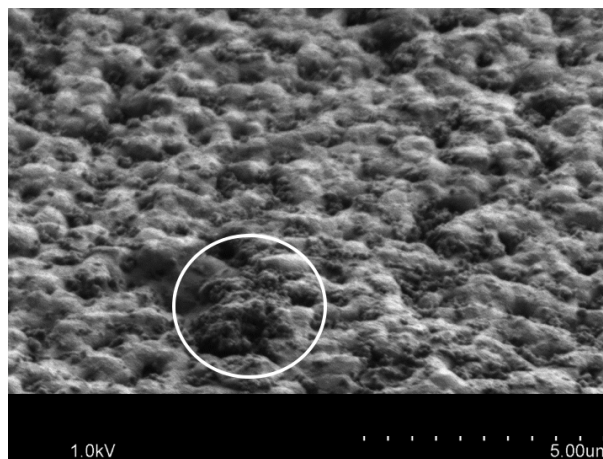
Fig. 3.8 shows the top view of the pure copper reference paste and of paste *D*, where dark agglomerations instead of pores are visible.

In fig. 3.9 the cross sections of the reference paste and paste *D* are shown. The pores of

paste *D* seem to include graphene flakes. Hence a FIB cut of this sampe was done for further investigations.

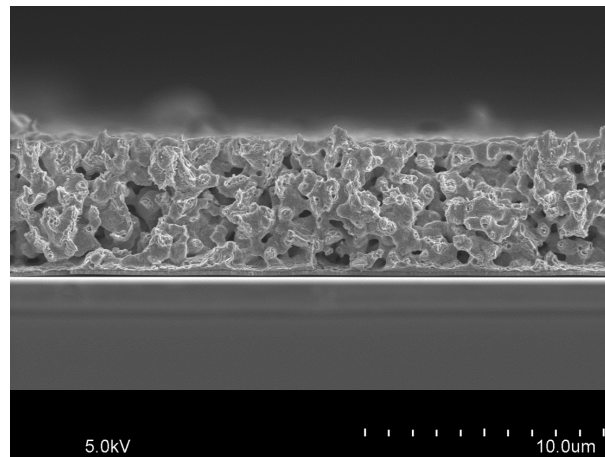


(a)

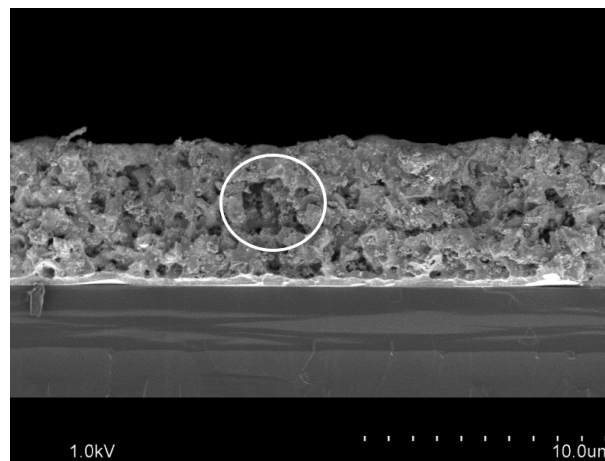


(b)

Figure 3.8: (a) Top view of pure copper reference paste. (b) Top view of paste D.



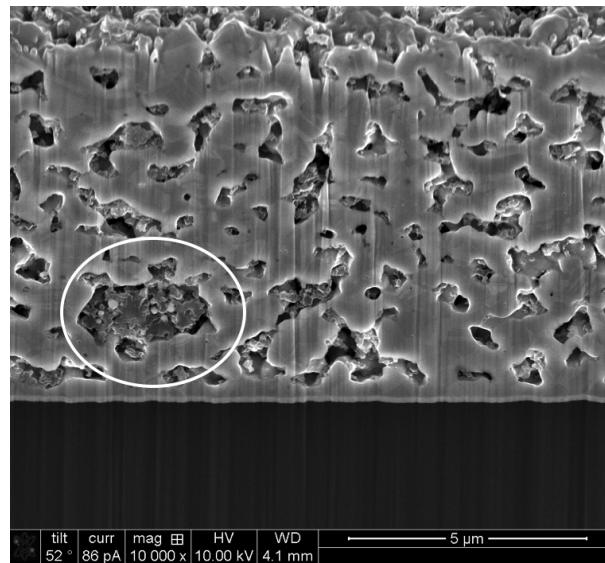
(a)



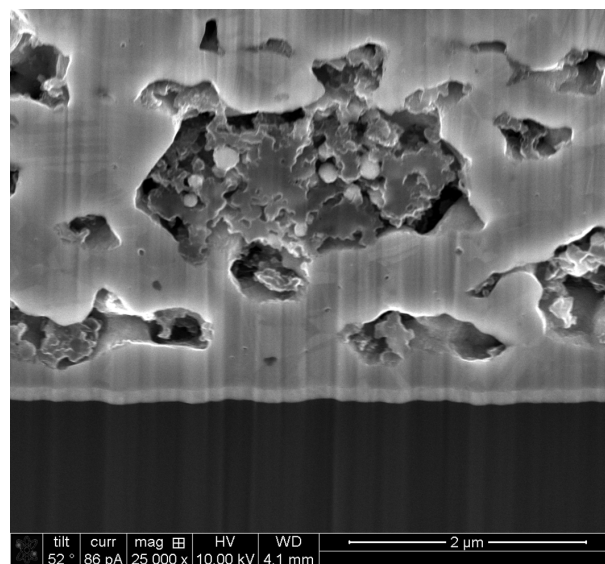
(b)

Figure 3.9: (a) Cross section of pure copper reference paste. (b) Cross section of paste D.

The agglomerated graphene is better visible using a FIB cut for sample preparation before investigating the sample in the SEM. The results are shown in fig. 3.10. Subfig. 3.10(b) shows the magnification of the marked region in subfig. 3.10(a).



(a)



(b)

Figure 3.10: (a) SEM of FIB cut of paste D. (b) Magnified graphene agglomeration.

Since graphene is deposited inside the pores, the porosity of the composite is expected to decrease compared to the pure copper paste. Using Archimedes' method as described in ch. 2.4.1.4, the graphene content is not considered, as only the density of copper is used for the calculation. To calculate the porosity *including* the graphene content using such a gravimetric method, it is necessary to know the weighed volume of copper and graphene. Subsequently, it is possible to subtract the weighed volume from the calculated volume to determine the volume of the pores. The ratio of pore volume and total volume can be used to calculate the porosity value. To calculate the volume of graphene, the density of graphite

was used as an approximation.

The porosity results considering graphene are similar to those not containing graphene which indicates that for such small wt.-% of graphene, Archimedes' method can be used in the same way as for pure copper materials to get basic information about the porosity of the investigated paste. For paste *D* the porosity equals  $30 \pm 2 \%$ .

The Raman spectroscopy detects multiple layer graphene, observable due to the ratio of the *2D-peak* and the *G-peak*, which is smaller than 1. Further information can be seen in fig. 3.11. In the upper part of fig. 3.11 the surface of the investigated sample is shown. On the right side the area is colored referring to the measured spots. Red spots indicate mono layer graphene, blue and violet spots multiple layer graphene.

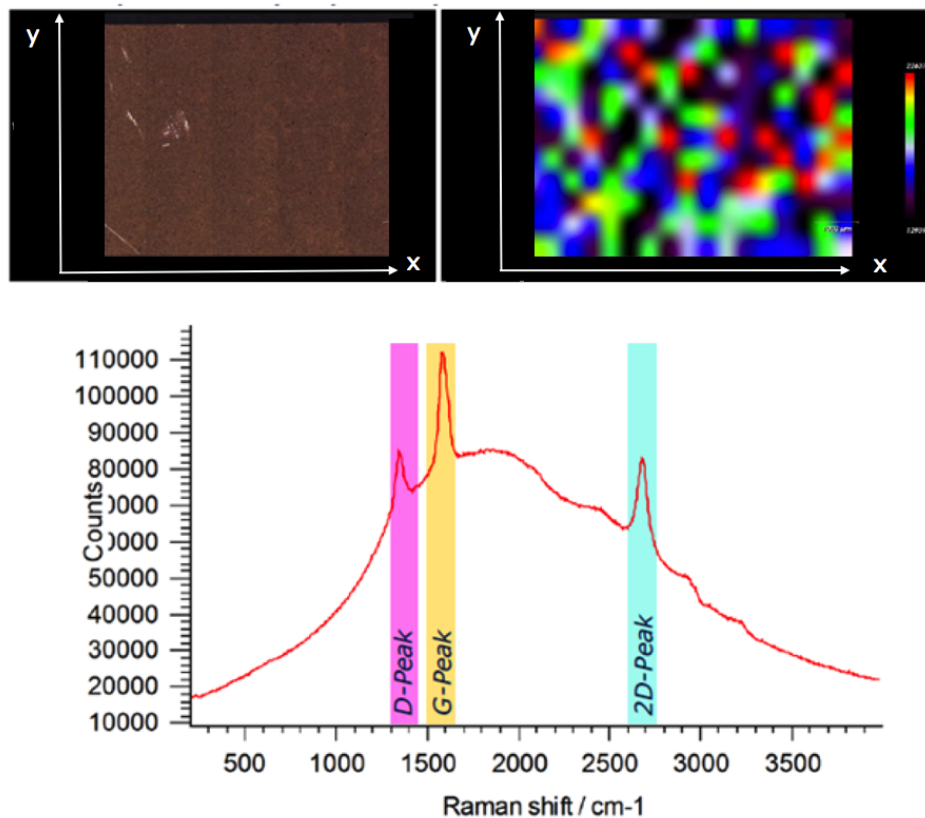


Figure 3.11: Raman spectrum of paste D.

The literature value of the CTE of bulk copper is around  $\alpha = 16.5 \cdot 10^{-6} \text{ K}^{-1}$ . Using thermo-mechanical analysis (TMA) for CTE measurements, the results show that there is no influence of the graphene content on the CTE.

For sample preparation the paste was printed on a silicon wafer which had been chemically pretreated (coating of hexamethyldisilazane, *HMDS*) to obtain a hydrophobic behavior. This is a method to provide thin graphene-copper films after curing which are required for the

thermomechanical analysis tool.

Fig. 3.12 shows measurements of paste *D* with results for the CTE  $\alpha = 14\text{-}18 \cdot 10^{-6} \text{ K}^{-1}$ . The dotted and solid lines equal the two measurement cycles. The green lines show the dimensional change of the sample during heating up to 250 °C. Additionally, the CTE value  $\alpha$  for each temperature is given by the blue line.

The dimensional change of the sample during heating is due to molecules gaining higher kinetic energy and moving further away from each other. The CTE ( $\alpha$ ) is given relative to the sample's original scale and the change in temperature.

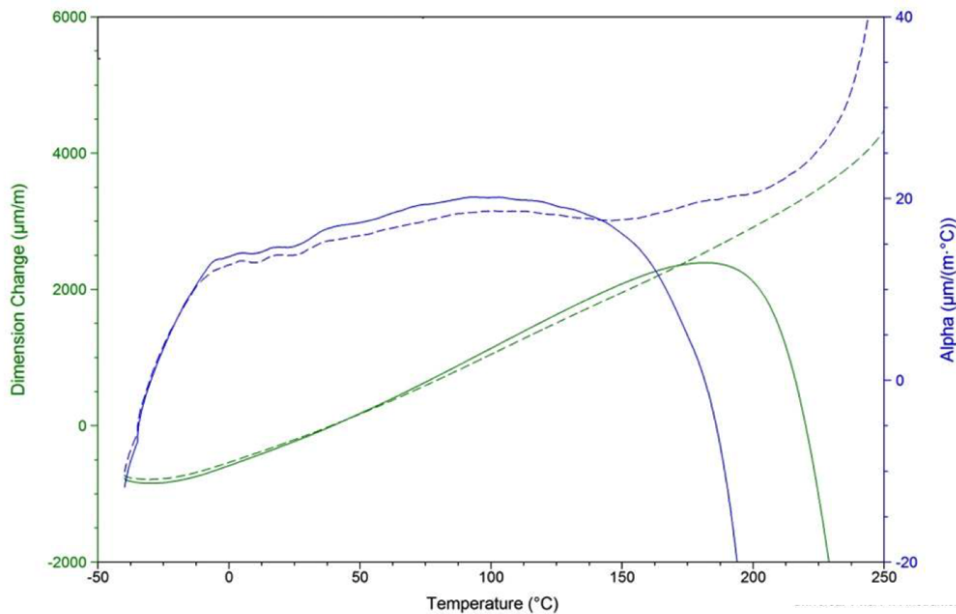


Figure 3.12: CTE measurements of paste D.

The stress behavior of paste *D* was investigated too. The stress difference over one temperature cycle between room temperature and 400 °C as well as the stress at room temperature are much higher than for the self-mixed pastes (see tab. 3.5).

The stress measurement data and the relevant results can be seen in fig. 3.13 and tab. 3.8. Curves *h1* and *h2* show the two heating steps up to 400 °C. The stress behavior of paste *D* is similar during *cooling 1* (after the first heating step) and *cooling 2* (after the second heating step), plotted as lines *cooling 1,2*.

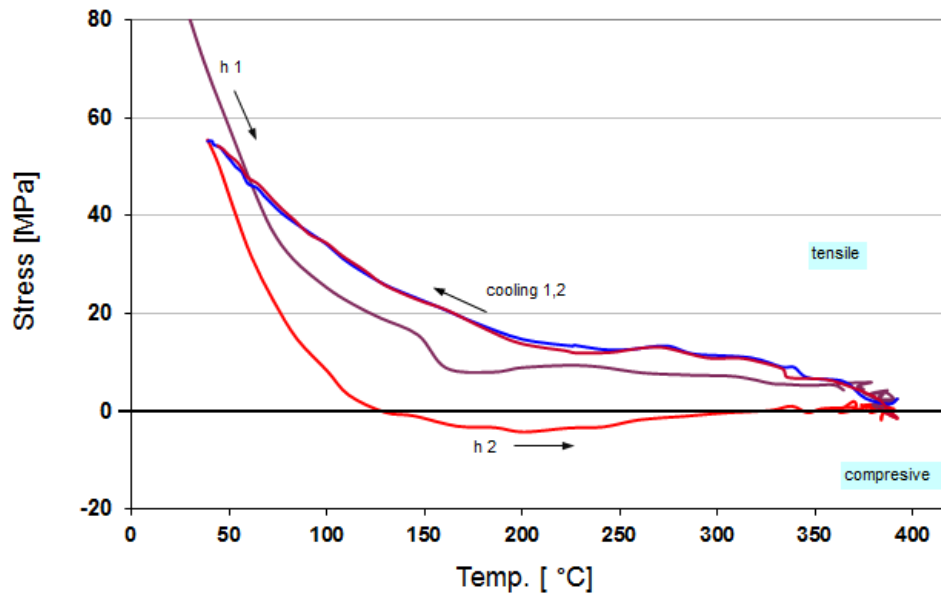


Figure 3.13: Stress measurements of paste D.

Table 3.8: Results of stress measurements of paste D.

paste	$\sigma_{\min-\max}$ / MPa	$\sigma_{RT}$ / MPa
paste D ( <i>B2FH</i> )	59	54

Further, Young's modulus was determined by dynamic mechanical analysis (DMA). The samples were heated two times. The results are divided into storage and loss modulus. The storage modulus measures the stored energy (representing the elastic portion) and the loss modulus measures the energy dissipated as heat (representing the viscous portion). The measurement data is shown in fig. 3.14. The storage modulus contains information about the paste's Young's modulus and is plotted as green colored line in fig. 3.14. The maximum of the storage modulus, which is an indicator for the sample's Young's modulus, equals  $E = 26 \text{ GPa}$  and is thus much lower than that of bulk copper (literature value:  $E = 117 \text{ GPa}$ ).

The loss modulus (plotted as blue line) as well as the dissipation factor  $\tan \delta$  (plotted as red line) will not be relevant for subsequent comparisons.

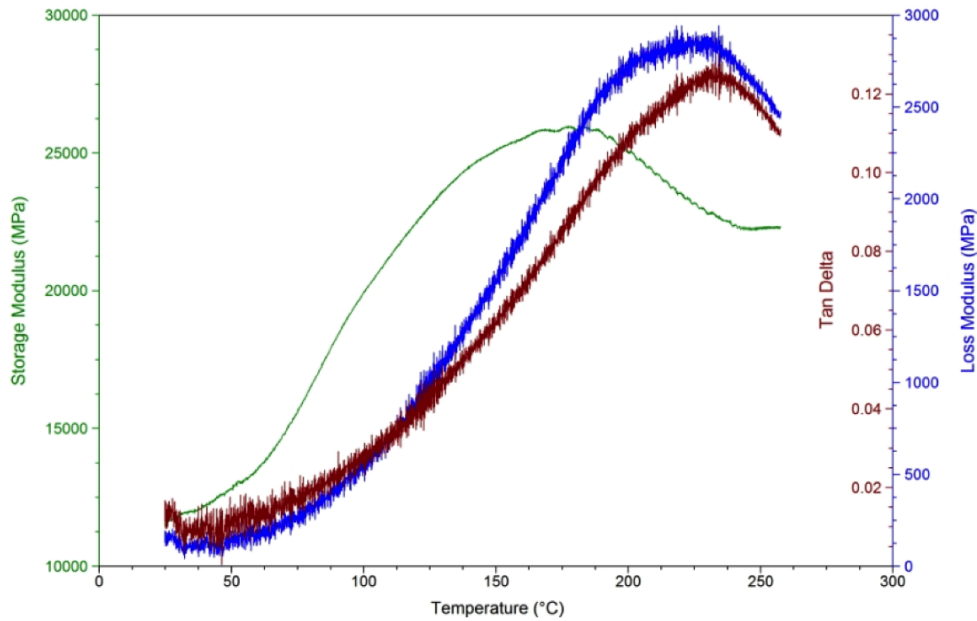


Figure 3.14: Dynamic mechanical analysis of paste D.

### 3.2.2.2 Micro-nano copper particle pastes with graphene content

Same as all the previous pastes, the micro-nano copper particle pastes with graphene, i.e. pastes *E* to *H*, were characterized regarding the aforementioned properties. The results were subsequently compared with the properties of the equivalent pure copper micro-nano particle paste *HSB3*.

The specific resistivity of each paste was again measured after a curing step (400 °C with a temperature holding time of 180 minutes). The results are shown in a boxplot, fig. 3.15, and tab. 3.9.

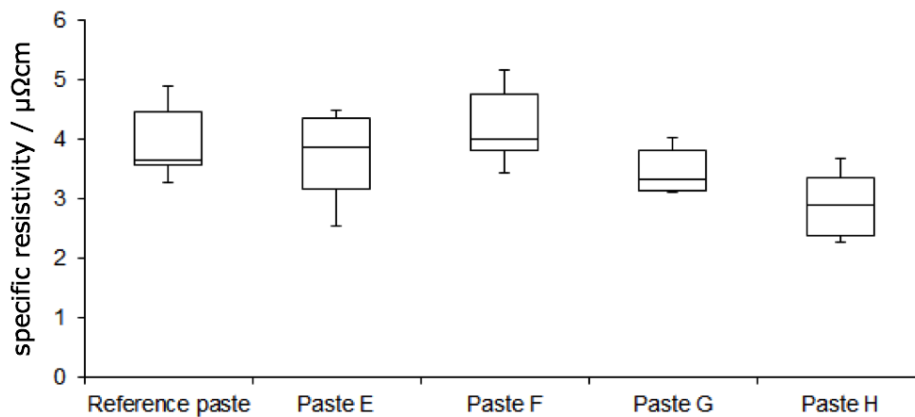


Figure 3.15: Specific resistivity values of micro-nano copper particle pastes with different graphene content and quality.

Table 3.9: Average specific resistivity values of pastes *E-H* compared to the reference paste

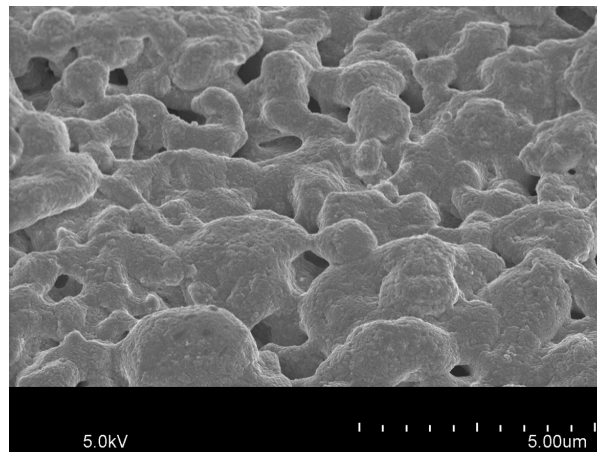
paste	average specific resistivity value / $\mu\Omega cm$
reference	$4.0 \pm 0.7$
E	$3.7 \pm 0.8$
F	$4.2 \pm 0.7$
G	$3.5 \pm 0.4$
H	$2.9 \pm 0.6$

Regarding the average specific resistivity values listed in tab. 3.9 it is noticeable that the copper-graphene combined pastes partially show better conductivity performance compared to the pure copper reference as opposed to the nano copper particle pastes containing graphene. The crucial criterium for choosing a paste for further analysis was again the specific resistivity performance. Hence, paste *H* (*B3FH*) is chosen due to its superior resistivity performance, while showing a mid-level porosity of  $32 \pm 2 \%$ . In this context it is necessary to mention that there is no clear explanation yet for the good resistivity results of the *few layer, high content* copper-graphene pastes.

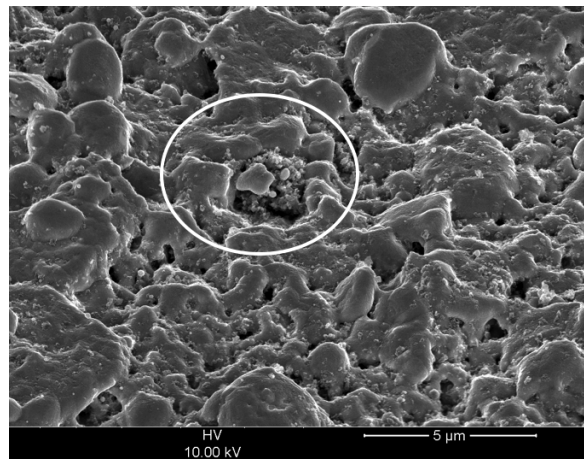
Comparing the micro structure of the pure copper reference paste and the copper-graphene paste *H* in a SEM image, the graphene content becomes visible. The agglomerated graphene is located in the pores from the surface down to the interface between the silicon substrate and the copper-graphene layer. The images of the surface and the cross section done using SEM analysis are shown in fig. 3.16 and fig. 3.17.

Fig. 3.16 shows the surfaces of the pure copper reference paste and paste *H*. The top view of paste *H* shows a porous structure, partially filled with agglomerations of graphene.

Fig. 3.17 shows the SEM images of the cross sections of the reference paste and paste *H*. As can be seen in subfig. 3.17(b), the graphene agglomerations fill the pores down to lower regions.

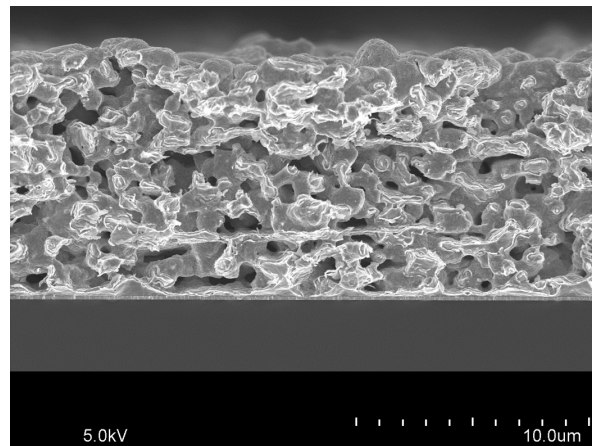


(a)

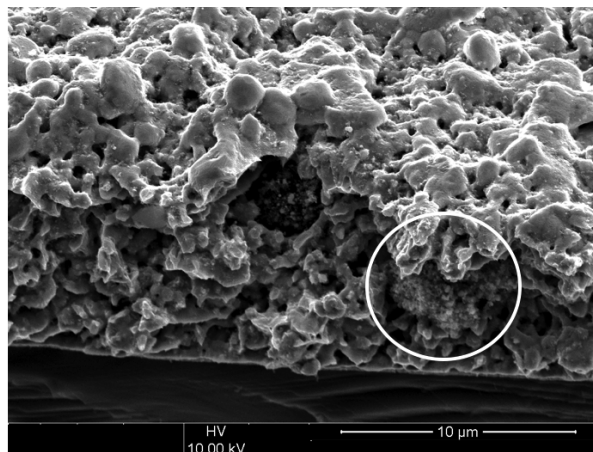


(b)

Figure 3.16: (a) Top view of pure copper reference paste. (b) Top view of paste H.



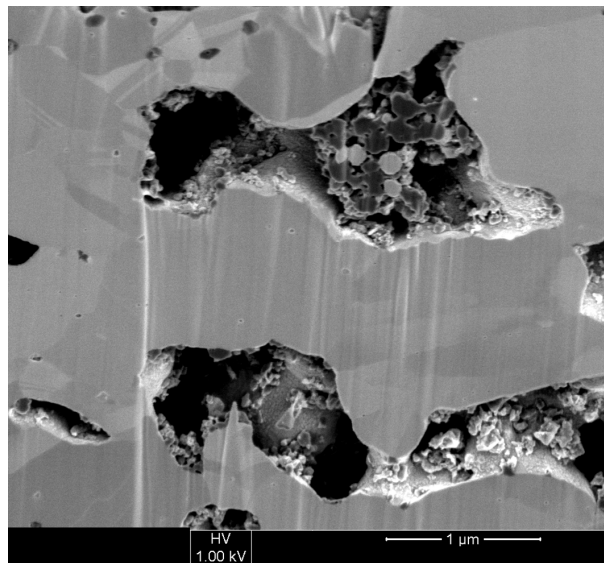
(a)



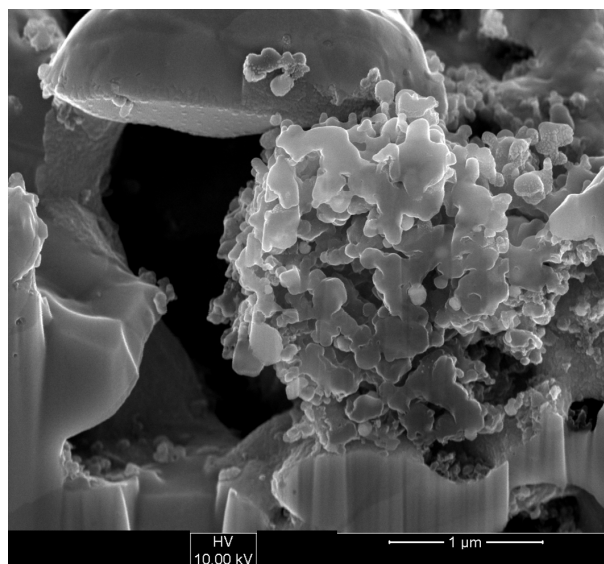
(b)

Figure 3.17: (a) Cross section of pure copper reference paste. (b) Cross section of paste H.

To make the graphene agglomerations easier to detect, a FIB cut of the samples of paste *H* was done previous to making further SEM images. The results are shown in fig. 3.18. Subfig. 3.18(b) shows a magnified graphene agglomeration of the upper part of subfig. 3.18(a). To ensure that the interpretation of the copper and graphene parts are correct, a complementary EDX analysis of the cross section of paste *H* was done (see fig. 3.19).



(a)



(b)

Figure 3.18: (a) SEM of FIB cut of paste H. (b) Magnified graphene agglomeration.

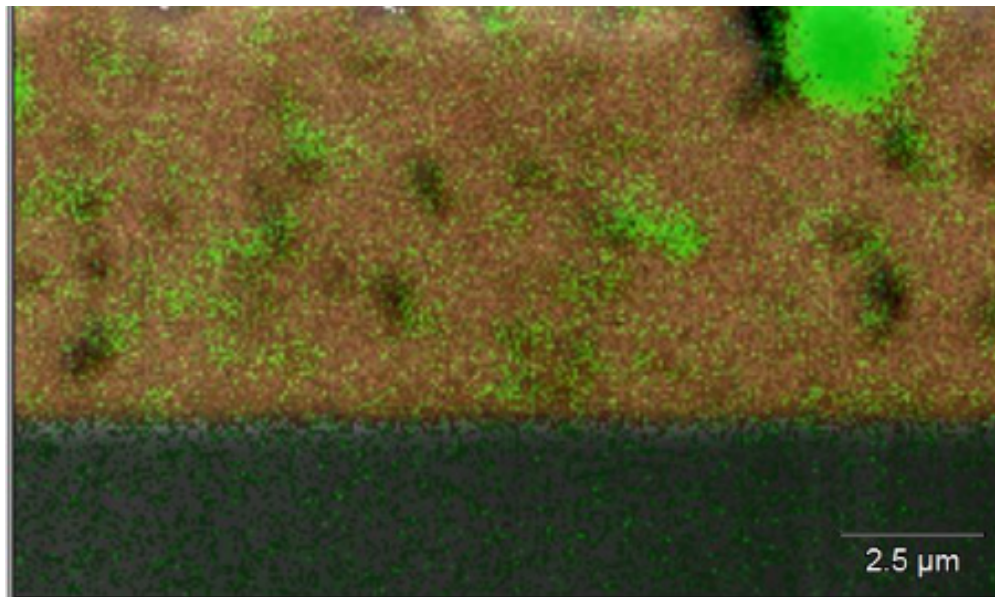


Figure 3.19: EDX-Analysis of paste H. Orange colored copper and green colored graphene/carbon located predominately in pores.

The graphene visible on the images before is detected as multiple layer graphene with a non negligible defect density, indicated by a sharp and high *D-peak*. The Raman spectrum can be seen in fig. 3.20. The upper part of fig. 3.20 shows the measured sample and the colored spots on the right side, indicating mono and multiple layer graphene.

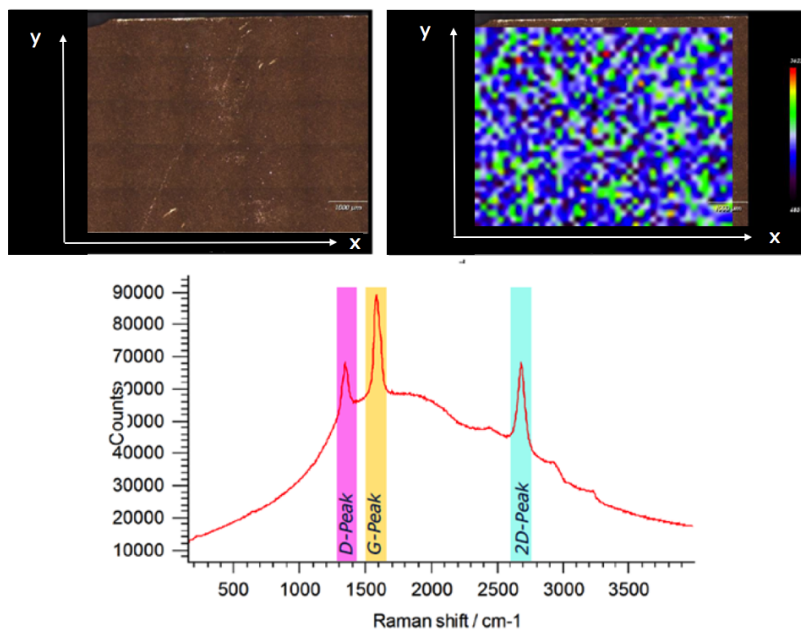


Figure 3.20: Raman spectrum of paste H.

One part of the characterization of paste *H*, same as for paste *D*, was the evaluation of the material's CTE using a thermomechanical analysis tool. After two measurement cycles, the results show similar values as the nano copper particle paste with graphene as well as the reference paste without graphene content. Additionally, with values around  $17\text{-}19 \cdot 10^{-6} \text{ K}^{-1}$ , the results are in a similar range as the literature value of bulk copper which is  $16.5 \cdot 10^{-6} \text{ K}^{-1}$ . The continuous and dotted lines in fig. 3.21 show the results of two measurement cycles. The dimensional change during the heating up to  $250 \text{ }^\circ\text{C}$  is plotted as green curve. The corresponding CTE data is plotted as blue curve.

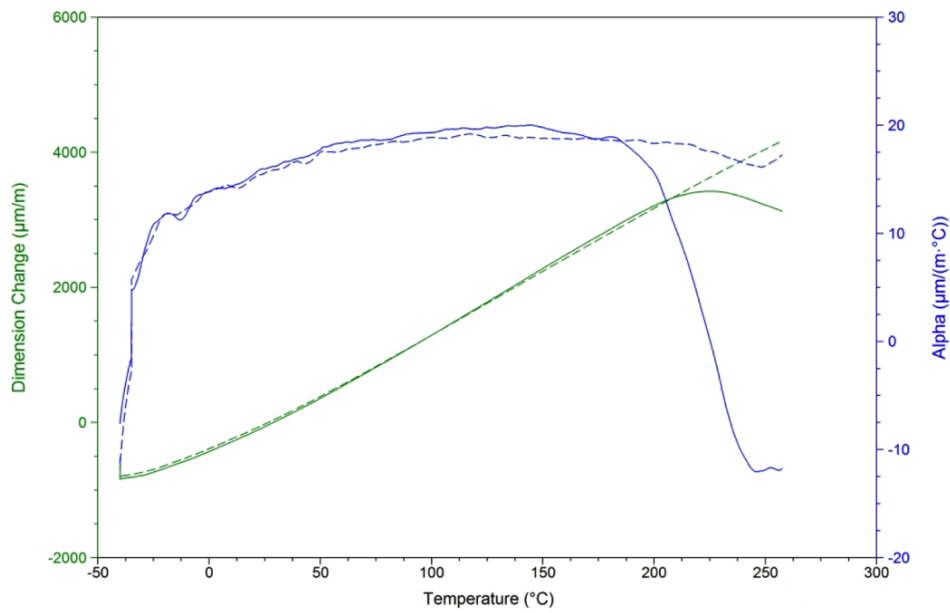


Figure 3.21: CTE measurements of paste H.

Furthermore, Young's modulus was measured using dynamic mechanical analysis. As opposed to the two measurement cycles used for TMA, in this case one heating cycle was performed on the sample. The measured values are shown in fig. 3.22, with a maximum storage modulus (green curve) of around  $E = 25 \text{ GPa}$ . This result is similar to the maximum storage modulus of the nano particle copper-graphene paste *D* ( $E = 26 \text{ GPa}$ ).

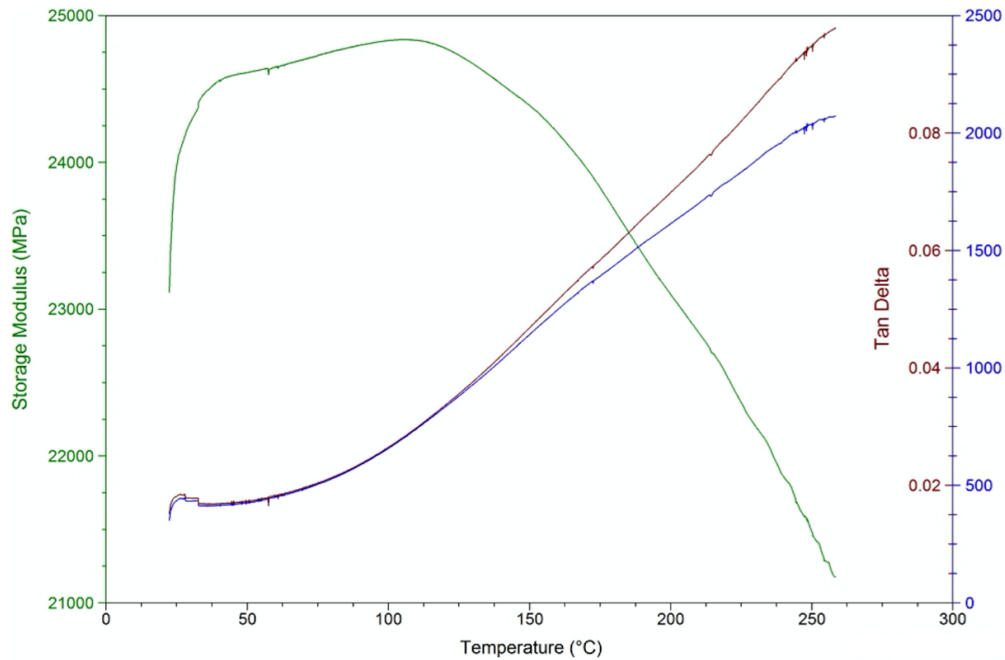


Figure 3.22: DMA results of paste H.

### 3.2.2.3 Characterization of remaining copper-graphene pastes

Previously described pastes were selected due to their respective specific resistivity performance. Since the results of the remaining pastes do not vary significantly and regarding the fact that they fall short of paste D's and H's superior conductivity performance, they were not analyzed in such detail as paste D and H. Still, the following chapter sums up further results of the remaining pastes.

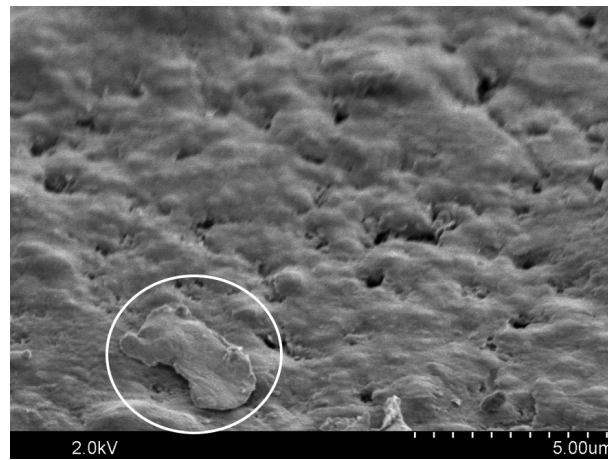
#### Nano copper particle pastes

All of the nano copper particle pastes containing graphene show similar results concerning the specific resistivity, from around  $3.5 - 5 \mu\Omega\text{cm}$ . The resistivity values did not give any clear information about a promising combination of the investigated graphene layer quality and content.

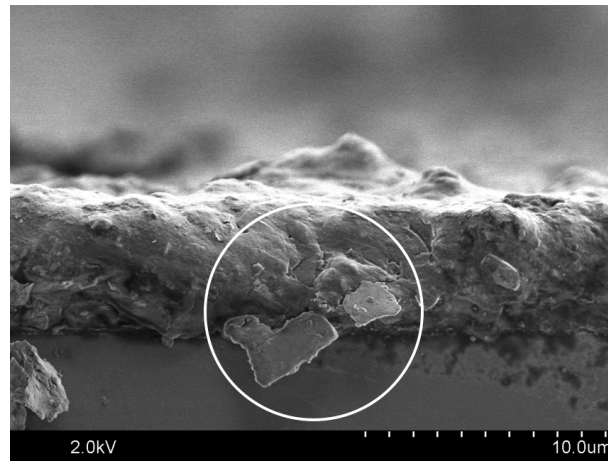
#### *Paste A:*

Comparing the microstructure of paste A (single layer graphene quality and low content) and paste D (few layer graphene quality and high content), it is notable that the layer of paste A material shows high density, probably due to organic paste residues that are not completely evaporated during curing. Furthermore large, spatially separated graphene flakes are visible. The SEM images of the surface and the cross section are shown in fig. 3.23. The large graphene flakes, mentioned before, can be seen in the marked regions of fig. 3.23. With a porosity of 40 % (measured using Archimedes' method) this paste shows higher porosity

than expected after evaluating the paste by a SEM.



(a)



(b)

Figure 3.23: (a) Top view of paste A. (b) Cross section of paste A.

The CTE measurements results in  $15-17 \cdot 10^{-6} \text{ K}^{-1}$ , i.e. similar to the other pastes and the bulk copper value.

The Raman analysis detected high defect density and partially monolayered graphene.

The stress measurements show results comparable to the stress values of, for example, paste *D*, as can be seen in tab 3.10.

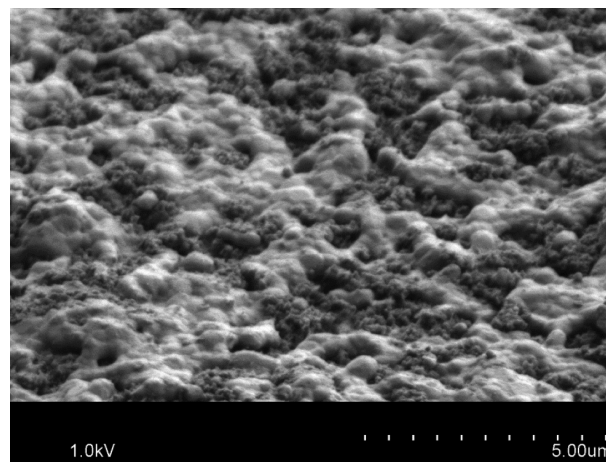
Table 3.10: Results of stress measurements of paste A.

paste	$\sigma_{\text{min-max}} / \text{MPa}$	$\sigma_{\text{RT}} / \text{MPa}$
paste A ( <i>B2SL</i> )	57	50

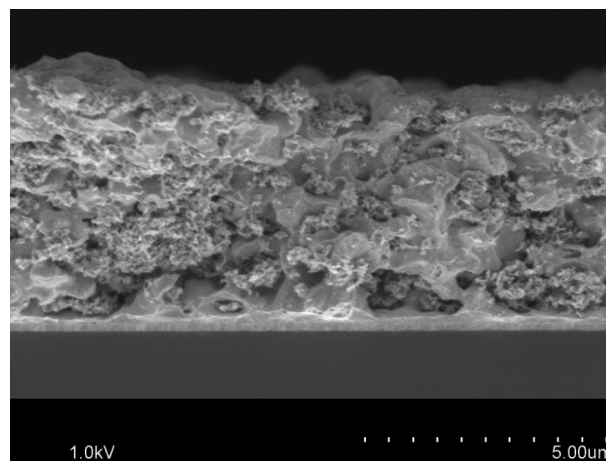
*Paste B:*

Paste B (single layer graphene quality and high content) was almost unprintable with the standard printing parameters due to its unusual, inhomogeneous texture and viscosity. Additionally, paste B did not show the expected paste roll behavior during printing. Hence, the wafers were not totally covered with paste.

The micro structure of paste B shows distributed graphene on the top and all the way down to the silicon interface. Although this paste only differs from paste A in the amount of the contained graphene, the micro structure looks very different. Fig. 3.24 shows the surface and the cross section of paste B. The agglomerated graphene is visible as dark material filling the pores.



(a)



(b)

Figure 3.24: (a) Top view of paste B. (b) Cross section of paste B.

Further measurements show similar results as the paste before (paste A). The CTE of paste B is in the same range again, i.e. between  $15\text{-}20 \cdot 10^{-6} \text{ K}^{-1}$ . Raman analysis shows a high

defect density and multiple layer graphene.

*Paste C:*

This paste had the second best specific resistivity result,  $3.9\mu\Omega cm$ , while showing medium porosity ( $28 \pm 4\%$ ). No SEM images are provided for paste *C*.

Further measurement methods such as Raman analysis show a spectrum without sharp peaks and a high defect density. Thus it is difficult to determine the type of graphene.

### Micro-nano copper particle pastes

Opposed to the nano copper particle pastes, the micro-nano copper particle pastes show specific resistivity results in the same range as the reference paste without graphene, but with the tendency to lower resistivity values. Same as for the nano copper particle pastes with graphene, the micro-nano copper particle pastes show the same pattern regarding graphene combinations. The best resistivity values were achieved by combination of *few layer graphene* and *high content* (manufacturer specification). The highest and consequentially worst specific resistivity values were obtained evaluating the *single layer* and *high content* copper-graphene pastes.

*Paste E:*

Paste *E* had a better conductivity performance at an average porosity of  $40 \pm 2\%$  than the reference paste (porosity:  $33 \pm 8\%$ ). Investigating the micro structure of this paste, it is remarkable that very thin graphene flakes are visible on the surface (bright spots) which show no adhesion to the copper system (see fig. 3.25).

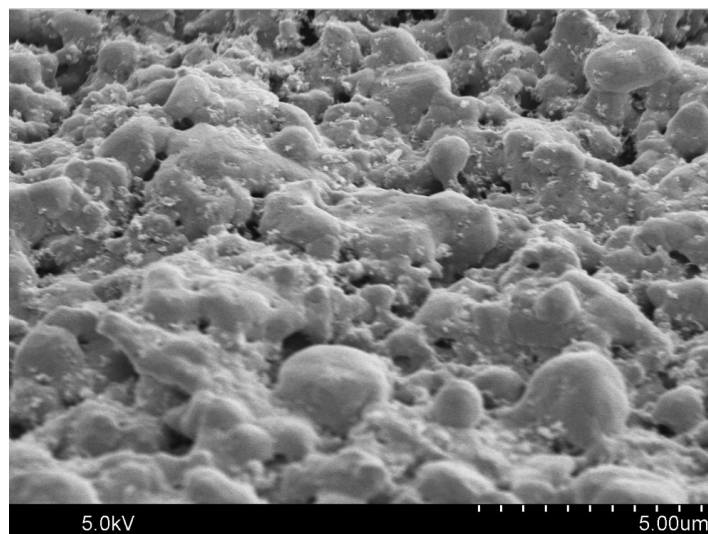


Figure 3.25: Top view SEM image of paste E.

Raman analysis detected a high defect density and multiple layer graphene. Furthermore, TMA results are in a range of  $18\text{-}22 \cdot 10^{-6} \text{ K}^{-1}$ , thus slightly higher than the CTE of the other pastes. Young's modulus, i.e. the maximum of the storage modulus, equals  $E = 22 \text{ GPa}$ .

*Paste F:*

Paste *F* shows the highest resistivity values, even higher than the reference paste, in spite of a similar average porosity ( $32 \pm 3 \%$ ) compared to the reference paste ( $33 \pm 8 \%$ ). Since paste *F* showed the worst conductivity performance, this paste had the lowest priority of all the pastes. No SEM images of this paste are provided.

The Raman spectrum clearly shows a high defect density and multiple layer graphene that reaches, as well as in all of the other pastes, down to the interface of the silicon substrate.

The CTE of paste *F* is within a range of  $15\text{-}18 \cdot 10^{-6} \text{ K}^{-1}$ . The highest value of the DMA measurement is close to  $E = 19 \text{ GPa}$ , which is the lowest value of Young's modulus observed while characterizing these pastes.

*Paste G:*

The micro structure of paste *G* is very similar to the micro structure of paste *E*. Very thin graphene flakes which are not noticeably bonded or rather integrated in the copper network are visible as small bright spots in fig. 3.26.

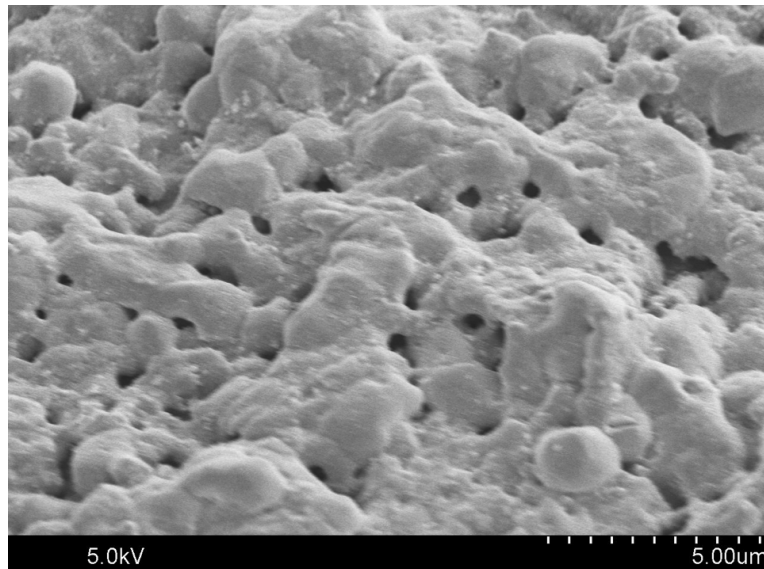


Figure 3.26: Top view SEM image of paste G.

Raman analysis again showed a high defect density and low signal intensity. Therefore it is difficult to interpret the Raman spectrum concerning the graphene quality.

The CTE of paste *G* equals values within a range of  $14\text{-}17 \cdot 10^{-6} \text{ K}^{-1}$ . The maximum value

of the storage modulus was measured by DMA and is close to  $E = 24 \text{ GPa}$ .

### 3.3 Raman spectroscopy of the silicon substrate

As described in ch. 2.4.7.1, Raman spectroscopy can further be used to determine the stress state in the silicon substrate induced by manufacturing processes, e.g. thinning, wafer metallization and so on. The aim of the following trials was to quantify the difference between metallization methods regarding the stress induced to the silicon substrate.

Initially, the  $725 \pm 25 \mu\text{m}$  thick silicon substrate was annealed at  $700 \text{ }^\circ\text{C}$  to release residual stresses prior to the manufacturing processes. Subsequently the generally used stack was built up on the wafer. As a reference, silicon wafers without metal stack (wafer 1 and 2) and silicon wafers with the sputtered metal stack, but without a printed top metallization (wafer 3 and 4) were measured. The sputtered metal stack includes  $150 \text{ nm}$  of *TiW* and  $150 \text{ nm}$  of *Cu*.

The following metallization methods were compared regarding stress induction:

- ECD copper (electrochemical deposition)
- sputtered copper
- LPNC copper (low porosity nano crystalline)
- printed copper

The measurements were done using a laser of  $633 \text{ nm}$  wavelength. Higher wavelengths show a stronger Raman effect, but also strong fluorescence. To prevent disruptive fluorescence, a laser of smaller wavelength could be used, but this would result in a smaller Raman effect. The reference wafers and the metallized wafers were measured successively to avoid a change in accuracy related to varying measurement conditions. For the mapping,  $4 \times 4$  spots of different wafer areas were done. Lasers in the range of red light show a penetration depth into the silicon substrate of about  $4 \mu\text{m}$ .

The following results were provided by *CTR Carinthian Tech Research AG*.

The metallization methods and corresponding layer thicknesses are listed in tab. 3.11. The results of the Raman stress measurements are shown in fig. 3.27 and fig. 3.28. Fig. 3.27 and fig. 3.28 show the stress states measured for every wafer listed in tab. 3.11 including error bars. Additionally, the stress states are characterized as compressive or tensile states, depending on the direction of the data bar.

Table 3.11: Overview of wafers characterized by Raman spectroscopy.

wafer number	metallization method	layer thickness / $\mu\text{m}$
5	ECD	15
6	ECD	15
7	ECD	30
8	ECD	30
9	LPNC	15
10	LPNC	15
11	LPNC	20
12	LPNC	20
13	LPNC	25
14	LPNC	25
15	LPNC	30
16	LPNC	30
17	PVD	1
18	PVD	1
19	PVD	5
20	PVD	5
21	Printed Cu ( <i>CP</i> )	15
22	Printed Cu ( <i>CP</i> )	15
23	Printed Cu-graphene ( <i>B3FH</i> )	8

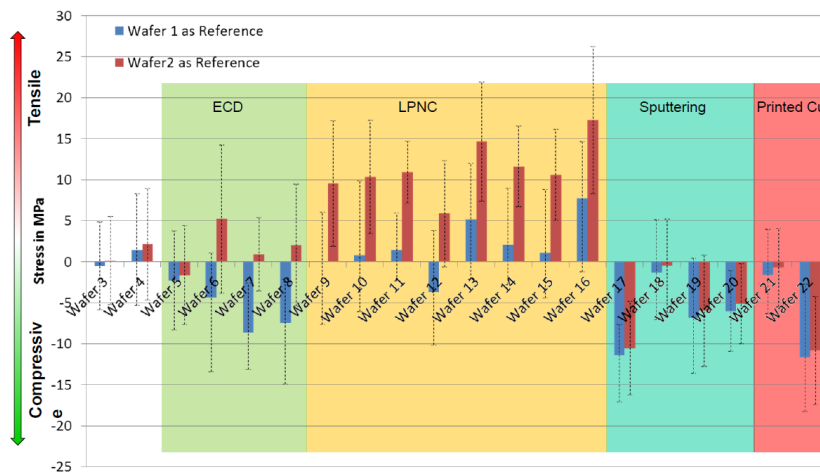


Figure 3.27: Stress states of silicon substrate after different methods of metallization deposition.

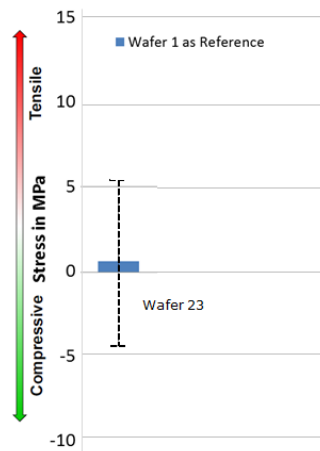


Figure 3.28: Stress states of silicon substrate after processing of paste H.

Since the measurement data partially shows very low stress states below  $5 \text{ MPa}$  which are usually not identified as stress states with a significant measurable effect, it has to be assumed that there is some inaccuracy in the experimental setup. The main reason for detecting such low stress values could be the thickness of the silicon substrate. Other experiments related to that topic show that wafers of a thickness around  $300 \mu\text{m}$  result in appropriate measurement data.

Due to unreliable results, this experiment should be repeated after thinning of the wafers. At the current state of knowledge it is not possible to evaluate the data in a meaningful way. Nevertheless, this method has a high potential for the measurement of stress on Si-wafer induced by metal or other layers on top.

## Chapter 4

# Summary and Conclusion

It could be shown in this thesis that adding graphene to copper paste systems mainly changes the micro structure of the solidified metal layer. Further properties such as electrical/thermal conductivity, the coefficient of thermal expansion, stress behavior and Young's modulus remain in the same value range as the equivalent pure copper pastes.

Furthermore, the results of the investigated copper-graphene pastes show that the influence of different available graphene qualities, i.e. graphene layers, is not as strong as assumed. However, the graphene content is essential for the physical properties of stencil printed porous copper-graphene pastes. Experiments showed that a content of, e.g., 5wt.-% graphene decreases the electrical conductivity performance of the copper-graphene network enormously. Contents less than or equal to 1 wt.-% result in similar physical properties as obtained for pure micro-nano and nano copper particle pastes. Regarding the provided pastes, the nano as well as the micro-nano copper particle pastes, combined with *few layer* graphene and *high content* achieved the best resistivity values.

Additionally, it has to be considered that a curing process was used which had been previously optimized for a certain pure copper paste, i.e. without graphene. The curing process itself is the most influential step during processing with regard to the physical properties of the final metallization layer. Since this process was not adapted to a copper-graphene compound, it is not ensured that the investigated pastes were processed in the best possible fashion. Generally, low-temperature curable pastes are aimed to provide a wider range of applications. Due to the fact that the used basic systems of copper pastes equal high-temperature curable pastes, there was no possibility to process the copper-graphene pastes at lower temperatures, which possibly would have been advantageous to enhance the properties of graphene such as electron mobility. Another hypothesis for not achieving significantly improved electrical conductivity results by adding graphene to the copper system could be that the graphene changes from being  $sp^2$ -hybridized to  $sp^3$ -hybridized carbon atoms by binding with an hydrogen atom during the curing process. Since the good electrical conductivity of graphene is based on its

$sp^2$ -hybridization, the curing process, which is necessary to achieve well conducting porous copper networks, would lower the electrical conductivity of graphene. Hence, there would be no possibility to optimize the porous copper layers by adding graphene, without changing the copper paste system or the curing step. The hybridization of graphene could be analyzed by using x-ray photoelectron spectroscopy (XPS). Further it should be considered, if the amount of graphene is high enough to generate a mono layer of graphene bonded to the copper network, which would also improve the electrical conductivity of the system.

Summarizing, it has to be stated that the method of adding graphene by stirring dissolved graphene powder into a copper paste does not lead to favorable results. In this case, amorphous instead of mono or multiple layer graphene is detected by use of Raman spectroscopy. All of the externally provided micro-nano as well as the nano particle copper-graphene pastes showed mono or rather multiple layer graphene, which changes the copper micro structure by graphene agglomeration in the pores. This microstructural change has no clear influence on the physical properties, as would have been expected. Physical properties, i.e. the coefficient of thermal expansion, Young's modulus and the stress behavior are comparable to the reference pastes without showing any noticeable increase or decrease in performance.

The Raman spectroscopy measurements regarding the stress states in the silicon substrate induced by different metallization methods could not be evaluated reliably due to the high thickness of the silicon substrate. The obtained stress values were too low to draw any significant conclusions.

As further steps, initially the development of pure, i.e. graphene-free, micro-nano and nano copper particle pastes has to be forced to obtain more satisfying layer properties of the base material, i.e. mainly lower specific resistivity values at similar porosity as well as higher layer thickness, low-temperature curability and an ensured complete removal of organic components during the curing process without surface discolorations.

Based on this and due to the fact that the pure copper pastes showed a similar performance regarding the physical properties, it can be concluded that copper-graphene compound pastes could be produced and processed using the methods described in this work. Secondly, to possibly enhance the performance of copper-graphene pastes compared to their equivalent pure copper pastes, optimization concerning the printing process, i.e. modification of the printing parameters, and especially the curing process has to be done.

# Appendix

Overview of measured results in tab. 4.1. Copper-graphene pastes are compared to the corresponding pure copper pastes (reference value).

The figures related to the results are shown below, fig. 4.1 - fig. 4.5.

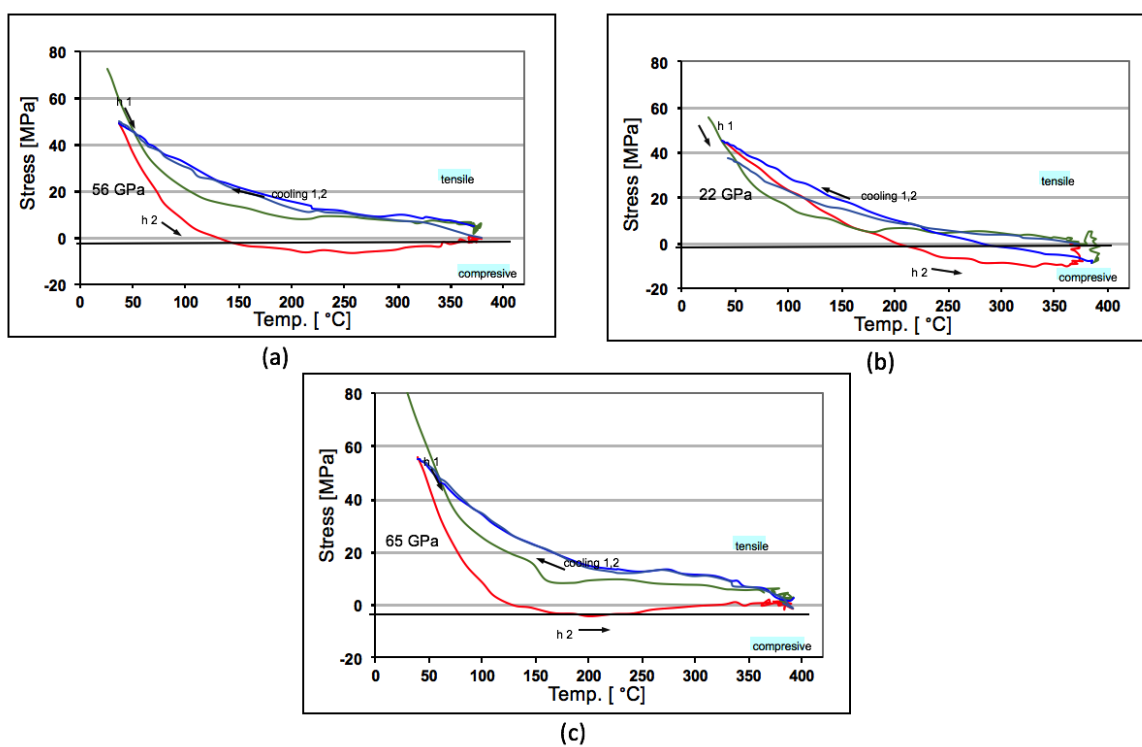


Figure 4.1: Stress measurements of paste A (a), paste B (b) and paste C (c).

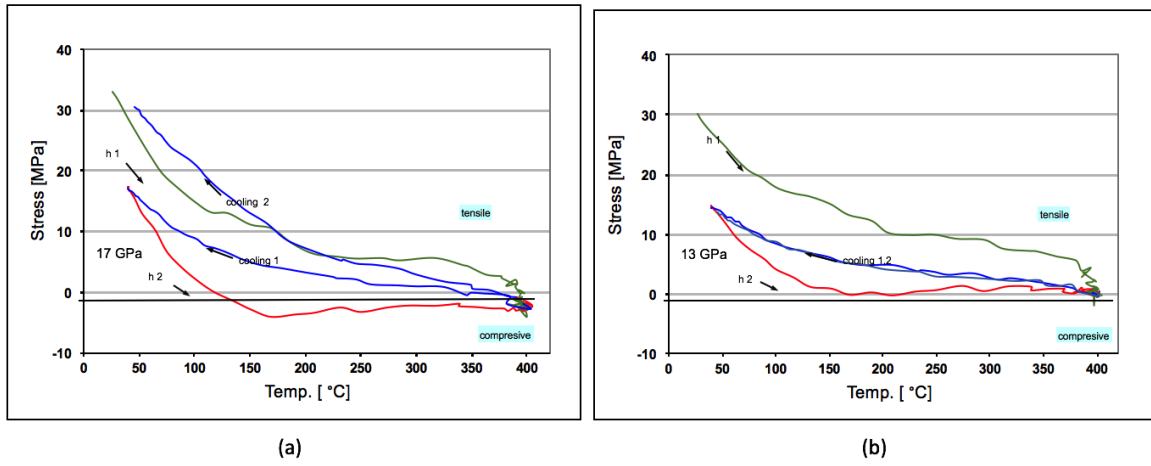


Figure 4.2: Stress measurements of CP with 1 wt.% materials grade graphene (a) and CP with 5 wt.% materials grade graphene (b).

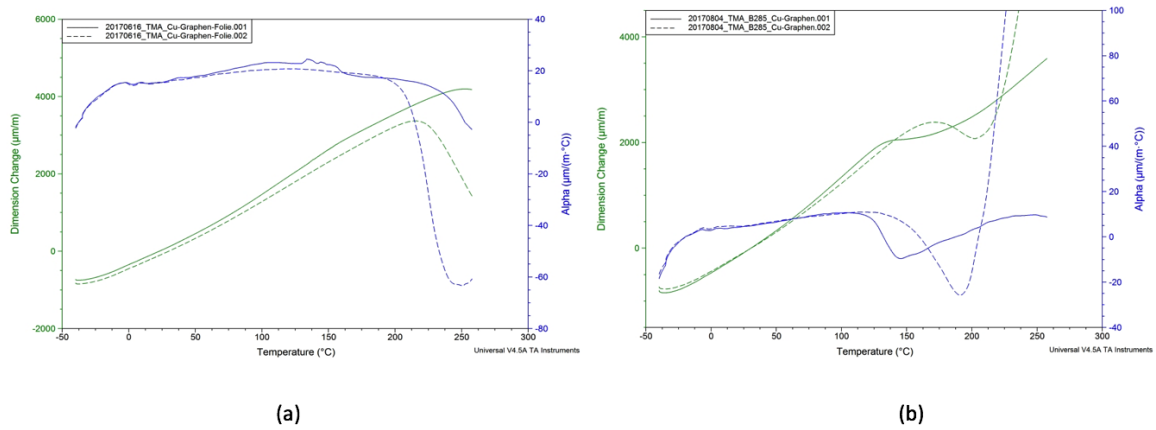


Figure 4.3: CTE measurements of paste A (a) and paste B (b).

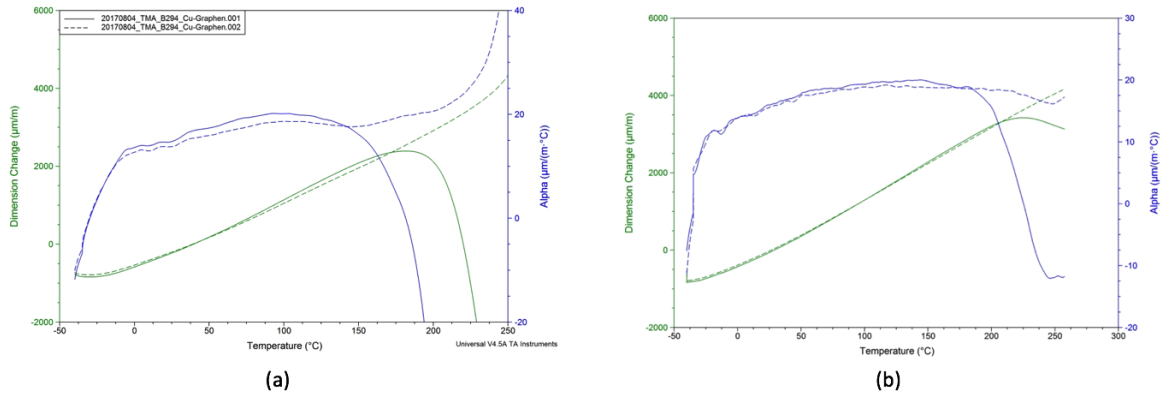


Figure 4.4: CTE measurements of paste *D* (a) and paste *H* (b).

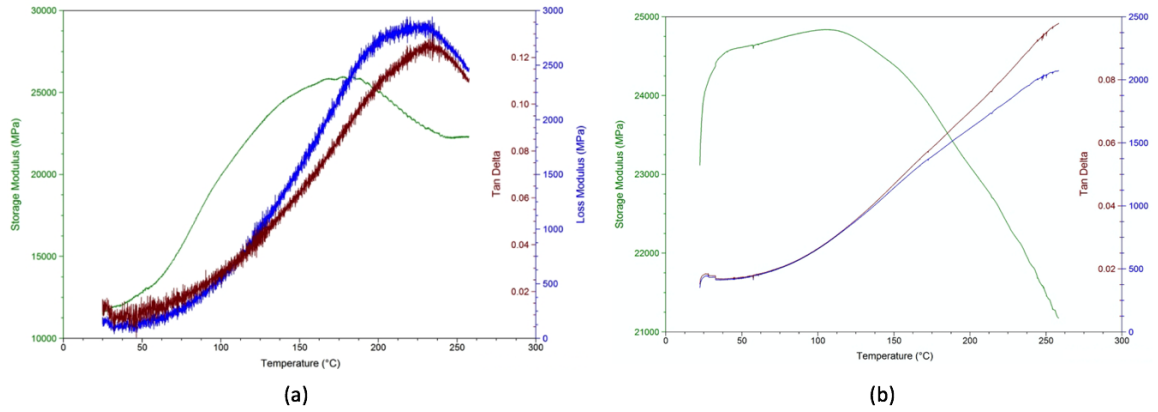


Figure 4.5: Young's modulus measurements of paste *D* (a) and paste *H* (b).

Table 4.1: Overview of measured results.

paste	layer thickness / $\mu\text{m}$ (reference value)	specific resistivity / $\mu\Omega\text{cm}$ (reference value)	porosity / % (reference value)	stress / MPa (reference value)	CTE / $10^{-6} \text{ K}^{-1}$ (reference value)	Young's modulus / GPa (reference value)
2B3	$7.5 \pm 1.2$	$6.2 \pm 1.1$	$42 \pm 5$	-	-	-
3B3	$8.5 \pm 1.3$	$5.0 \pm 1.0$	$36 \pm 5$	-	-	-
4B3	$18.0 \pm 2.1$	$9.0 \pm 1.1$	$55 \pm 4$	-	-	-
5B2	$4.5 \pm 1.3$	$2.4 \pm 1.1$	$21 \pm 4$	-	-	-
5B3	$25.0 \pm 1.6$	$15.0 \pm 1.1$	$66 \pm 5$	-	-	-
HSB3	$11.0 \pm 2.8$ (8.5)	$4.0 \pm 0.7$ (5.0)	$33 \pm 8$ (36)	-	-	-
86B2	$5.0 \pm 1.2$ (4.5)	$3.1 \pm 1.3$ (2.4)	$25 \pm 5$ (21)	-	-	-
A (B2SL)	$6.5 \pm 1.7$ (5.2)	$4.1 \pm 0.7$ (3.1)	$40 \pm 7$ (24)	57	15-17	-
B (B2SH)	$7-8^*$ (5.2)	$5-6^*$ (3.1)	-	47	15-20	-
C (B2FL)	$6.2 \pm 1.3$ (5.2)	$3.9 \pm 0.5$ (3.1)	$28 \pm 4$ (24)	-	-	-
D (B2FH)	$6.7 \pm 1.1$ (5.2)	$3.4 \pm 0.4$ (3.1)	$30 \pm 2$ (24)	59	14-18	26
E (B3SL)	$8.6 \pm 1.2$ (11.3)	$3.7 \pm 0.8$ (4.0)	$40 \pm 2$ (37)	-	-	-
F (B3SH)	$9.7 \pm 1.6$ (11.3)	$4.2 \pm 0.7$ (4.0)	$32 \pm 3$ (37)	-	-	-
G (B3FL)	$7.8 \pm 1.4$ (11.3)	$3.5 \pm 0.4$ (4.0)	$27 \pm 3$ (37)	-	-	-
H (B3FH)	$7.6 \pm 1.3$ (11.3)	$2.9 \pm 0.6$ (4.0)	$32 \pm 3$ (37)	-	17-19	25
1 wt.% materials gr.	$10.5 \pm 1.9$	$5.8 \pm 0.3$ (4.5)	$42 \pm 3$	21 (30)	-	-
1 wt.% premium gr.	$10.7 \pm 1.9$	$5.8 \pm 0.3$ (4.5)	$44 \pm 5$	-	-	-
5 wt.% materials gr.	$11.0 \pm 1.6$	$8.5 \pm 1.8$ (4.5)	$39 \pm 3$	14 (30)	-	-

# Bibliography

- [1] Guo-Feng Chen Peisheng Liu Ph.D. *Porous Materials: Processing and Applications*. Butterworth-Heinemann, 1 edition, 2014.
- [2] M. Nanko (auth.) K. Ishizaki, S. Komarneni. *Porous Materials: Process technology and applications*. Materials Technology Series 4. Springer US, 1 edition, 1998.
- [3] Juan Pablo M. Florez, Marcia B.H. Mantelli, and Gustavo G.V. Nuernberg. Effective thermal conductivity of sintered porous media: Model and experimental validation. *International Journal of Heat and Mass Transfer*, 66:pp. 868–878, 2013.
- [4] Russell Goodall, Ludger Weber, and Andreas Mortensen. The electrical conductivity of microcellular metals. *Journal of Applied Physics* 100.
- [5] Erlin Zhang and Bin Wang. On the compressive behaviour of sinteredporous coppers with low to medium porosities—part i: Experimental study. *International Journal of Mechanical Sciences*, 47, 2005.
- [6] Madhuri Sharon, Maheshwar Sharon, Ashutosh Tiwari, and Hisanori Shinohara. *Graphene : an introduction to the fundamentals and industrial applications*. Advanced materials series (Scrivener Publishing). Wiley-Scrivener, 1 edition, 2015.
- [7] Mohammad Ali Rafiee. *Graphene-based Composite Materials*. PhD thesis, Rensselaer Polytechnic Institute, Troy, New York, 2011.
- [8] C. N. R. Rao and Ajay K. Sood. *Graphene: Synthesis, Properties, and Phenomena*. Wiley-VCH, 1 edition, 2013.
- [9] Ephraim M. Sparrow, John P. Abraham, and John M. Gorman. *Advances in Heat Transfer*, volume 48. Academic Press, 2016.
- [10] A. C. Ferrari et al. Science and technology roadmap for graphene, related two-dimensional crystals, and hybrid systems. *Nanoscale*, 7, 2015.
- [11] Robert Kay Marc Desmulliez. A review of stencil printing for microelectronic packaging. *Soldering & Surface Mount Technology*, Vol. 24:pp. 38–50, 2012.

- 
- [12] Markus Heinrici. Entwicklung und evaluierung von printing-prozessen zur erzeugung von leitfähigen strukturen auf si-wafern. Master's thesis, Technische Universität Graz.
- [13] Barbara Eichinger. Effects of curing processes on material properties of porous copper. Master's thesis, Vienna University of Technology, 2016.
- [14] Andreas Munding. *Interconnect Technology for Three-Dimensional Chip Integration*. PhD thesis, Ulm University, 2007.
- [15] Peter Wellmann. *Materialien der Elektronik und Energietechnik: Halbleiter, Graphen, Funktionale Materialien*. Springer Vieweg, 1 edition, 2017.
- [16] David G. Rethwisch William D. Callister. *Materials Science and Engineering An Introduction*. Wiley, 9 edition, 2013.
- [17] Rudolf Huebener. *Kristalle, Spielfeld der Elektronen*. Wiley-VCH, 2003.
- [18] Siegfried Hunklinger. *Festkoerperphysik*. Oldenbourg Wissensch.Vlg, 2007.
- [19] M. F. Ashby, Tony Evans, N. A. Fleck, Lorna J. Gibson, John W. Hutchinson, and H. N. G. Wadley. *Metal Foams: A Design Guide*. Butterworth-Heinemann, 1 edition, 2000.
- [20] Wei Zhou, Yong Tang, Rong Song, Lelun Jiang, K.S. Hui, and K.N. Hui. Characterization of electrical conductivity of porous metal fiber sintered sheet using four-point probe method. *Materials and Design*, vol. 37:pp. 161–165, 2012.
- [21] Gary L. Grove Jorgen Serup, Gregor B. E. Jemec. *Handbook of Non-Invasive Methods and the Skin, Second Edition*. Informa Healthcare, 2 edition, 2006.
- [22] Guido Kickelbick. *Chemie für Ingenieure*. Pearson Studium, 2008.
- [23] Professor Dr. Ludwig Reimer. *Scanning Electron Microscopy: Physics of Image Formation and Microanalysis*. Springer Series in Optical Sciences 45. Springer-Verlag Berlin Heidelberg, 2 edition, 1998.
- [24] Ludwig Reimer. *Image Formation in Low-voltage Scanning Electron Microscopy*. SPIE-The International Society for Optical Engineering, 1993.
- [25] H.C. Sharma, Rajesh Kharb, and Rajesh Sharma. *Comprehensive Physics for Engineers*. fourth edition.
- [26] Dusan Losic Krishna Kant Ph.D. and Zhiming M. Wang. *FIB Nanostructures*. Lecture Notes in Nanoscale Science and Technology 20. Springer International Publishing, 1 edition, 2013.

- 
- [27] North Carolina State University Lucille A. Giannuzzi. *Introduction to Focused Ion Beams: Instrumentation, Theory, Techniques and Practice*. Springer, 1 edition, 2004.
- [28] C. Michael Neag. Thermomechanical analysis in materials science. *Materials Characterization by Thermomechanical Analysis, American Society for Testing and Materials, Philadelphia*, pages pp. 3 –21, 1991.
- [29] Ernst Schmachtenberg Georg Menges Edmund Haberstroh, Walter Michaeli. *Werkstoffkunde Kunststoffe*. Hanser, Carl, 6. edition, 2011.
- [30] Kevin P. Menard. *Dynamic Mechanical Analysis: A Practical Introduction*. CRC Press, 2 edition, 2008.
- [31] R. Huang. *Stress and microstructural evolution of electroplated copper lms*. PhD thesis, Vienna University of Technology, 2012.
- [32] Bernhard Schrader. *Infrared and Raman spectroscopy: methods and applications*. Wiley-VCH, 1995.
- [33] Dr. Heribert Moser Dr. Josef Brandmüller. *Einführung in die Ramanspektroskopie*. Wissenschaftliche Forschungsberichte 70. Steinkopff-Verlag Heidelberg, 1 edition, 1962.
- [34] *Raman micro-spectroscopy as a non-destructive key analysis tool in current power semiconductor manufacturing*, volume 10210, 2017.
- [35] M. De Biasio, L. Neumaier, N. Vollert, E. Geier, M. Roesner, Ch. Hirschl, and M. Kraft. Determination of stress in silicon wafers using raman spectroscopy. 2015.
- [36] Andrea C. Ferrari. Raman spectroscopy of graphene and graphite: Disorder, electron–phonon coupling, doping and nonadiabatic effects. *Solid State Communications*, 143:pp. 47 – 57, 2007.